JAIST Repository
https://dspace.jaist.ac.jp/

Title	複合超音波断層画像を用いた動的輪郭モデルによる肺がん領域抽出に関する研究
Author(s)	Keatmanee, Chadaporn
Citation	
Issue Date	2018-03
Type	Thesis or Dissertation
Text version	ETD
URL	http://hdl.handle.net/10119/15325
Rights	
Description	Supervisor:小谷　一孔，情報科学研究科，博士

Japan Advanced Institute of Science and Technology

Breast Cancer Detection by Active Contour Model Utilizing the Integration of Ultrasonography Image Modalities

by

Chadaporn Keatmanee

Supervisor (s): Kazunori Kotani
Stanislav S. Makhanov

School of Information Science
Japan Advanced Institute of Science and Technology

March, 2018

Abstract

Active contours (snakes) are an efficient method for segmentation of ultrasound (US) images of breast cancer. However, the method produces inaccurate results if the seeds are initialized improperly (far from the true boundaries and close to the false boundaries). Therefore, we propose a novel method to overcome drawbacks of snakes including initialization sensitivity and noise robustness based on the fusion of conventional US image with Elastography and Power Doppler images. The integrated information extracted from the three types of images provides better initialization and more tolerate to noise, consequently, leads to better segmentation. The proposed fusion method (FM) has been tested against four state-of-the-art initialization methods on 90 ultrasound images from a database collected by the Thammasat University Hospital of Thailand. The ground truth was hand-drawn by three leading radiologists of the hospital. The reference methods were center of divergence (CoD), force field segmentation (FFS), Poisson Inverse Gradient Vector Flow (PIG), and quasi-automated initialization (QAI). Using a variety of measures, the results prove the following advantages of the FM. For the raw US images the percentage of correctly initialized contours of FM is 94.2% ,whereas, COD, FFS, PIG, and QAI are 0%, 0%, 26.7%, 42.2% respectively. Besides the proposed initialization method, we introduced a robust external force field applying to strong noise named fusion radial force (FRF). The combination of the fusion and radial force outperforms the Vector Field Convolution (VFC) and the Adaptive Diffusion Flow (ADF). The percentage of correctly converge to boundaries of tumors is 84.4% for FM, whereas, VFC and ADF are 56.62% and 43.30% respectively.

Keywords: breast cancer segmentation, initialization for active contours, ultrasound, Elastrography, Doppler

Acknowledgments

I first of all thank my advisers prof.Kazunori Kotani and prof.Stanislav S. Makhanov who have very kind supported and guided me throughout the period of my work and have been very generous helpful. I would also like to thank all committee members, Dr.Saowapak S. Thongvigitmanee, Dr.Toshiaki Kondo, and Dr. Pakinee Aimmanee for their valuable advices and suggestion to understand and improve my work.

I am thankful to my Thai, Japanese, and other national friends who assisted me in identifying relevant on living abroad and guided me throughout the period of my work including coding, presenting, and report writing.

I would like to thank, JAIST-SIIT dual degree program, my scholarship donor, Sirindhorn International Institute of Technology (SIIT), Japan Advanced Institute of Science and Technology (JAIST), and National Electronics and Computer Technology Center (NECTEC) for providing me this opportunity and supporting me financially. Furthermore, I would like to express my appreciation to Dr.Utairat Chaumrattanakul and Dr.Wanrudee Lohitvisate, radiologists in department of Radiology, the Thammasat hospital for providing me valuable guidance in breast cancer diagnosis and knowledge in ultrasonic imaging modalities for breast cancer scanning analysis including ground truth.

Contents

Abstract i

Acknowledgments ii

List of Figures vii

List of Tables x

List of Abbreviations xi

1 Introduction 1

- 1.1 Overview of active contour model in breast cancer detection using ultrasonography image modalities . . . 1
- 1.2 Research Problem and Motivations . . . 3
- 1.3 Research Vision, Purpose and Objectives . . . 4
- 1.4 Dissertation Scope . . . 5
- 1.5 Dissertation Outline . . . 5

2 Related work 9

- 2.1 Related Work . . . 9

3 Background 13

- 3.1 Introduction . . . 13
- 3.2 Applying Ultrasonography imaging modalities in breast cancer screening . . . 14
- 3.3 The integration of Ultrasonography imaging modalities in improving sensitivity and specificity . . . 15
  - 3.3.1 Conventional Ultrasound . . . 16

3.3.2 The integration of Ultrasonography imaging modalities in medical image processing 18
3.3.3 Segmentation of breast cancer 19
3.4 Active contour Model 19
3.4.1 Parametric Active Contour Model 20
3.4.2 Geometric Active Contour Model 20
3.4.3 An automatic initialization of parametric active contour model 20
3.4.4 An internal force of ACM. 21
3.4.5 An external force of ACM. 22

4 Ultrasonographic imaging modalities preprocessing and registration 25
4.1 Materials 25
4.1.1 Sequence of ultrasonic imaging modalities 25
4.1.2 Ground truth of conventional US 26
4.2 Preprocessing process 26
4.2.1 Image inpainting 26
4.2.2 Image resize 27
4.3 Image registration 27
4.3.1 Thin plates spline 27
4.3.2 Image registration between conventional US and Power Doppler 29
4.3.3 Image registration between conventional US and Elastography 29

5 Methodology 38
5.1 Introduction 38
5.2 Binarized process 40
5.2.1 Conventional US 40
5.2.2 Elastography 41
5.2.3 Power Doppler 42
5.3 Common area detection. 44
5.3.1 Soft intersection using distance transform algorithm 44
5.4 Estimation of an initial contour setting in conventional US 46
5.4.1 Hausdorff distance 47

5.4.2 Modified Hausdorff distance 47
5.4.3 Partial Hausdorff distance 47
5.4.4 Automatic initialization for ACM. 48
5.4.5 Automatic initialization and segmentation 48
5.4.6 Balloon radial force 50

6 Performance measures **56**
6.1 Contour based accuracy measures 56
6.2 Region based accuracy measures 57
6.3 Performance of the initialization procedure 57

7 Results and Discussion **59**
7.1 Evaluation and discussion 59
7.1.1 Impact of the radial force 60
7.1.2 Relative impact of different modalities 62
7.1.3 Limitations of the method 65

8 Conclusion and Futer Work **66**
8.1 Conclusion 66
8.2 Future work 67

Bibliography **81**

Publications **82**

A Minor research: Inferior alveolar canal segmentation in cone beam computed tomography images using an adaptive diffusion flow active contour model **83**
A.1 Introduction 84
A.2 Related Work and Theoretical Background 84
A.3 Theoretical Background 85
A.4 Inferior Alveolar Canal Segmentation 87
A.4.1 Materials 87
A.4.2 Image Enhancement 87
A.4.3 Segmentation and Tracking Process 87

A.4.4 3D Reconstruction 88

A.4.5 Data Analysis 91

A.5 Results and Discussion 92

A.6 Conclusions and Future Work 93

This dissertation was prepared according to the curriculum for the Collaborative Education Program organized by Japan Advanced Institute of Science and Technology and Thammasat University.

List of Figures

1.1 Over all process for improving performance of active contour model in breast cancer detection using ultrasonography image modalities 8

3.1 Color bar shows stiffness of a breast mass in Elastography. 17
3.2 US images in a patient at Thammasat university hospital show high suspicious of malignant mass. (a) Conventional US shows an irregular hypoechoic mass. (b) Elastography shows the entire mass as red and dark red. (c) Power Doppler shows increased vascularity. 18

4.1 The process of image preprocessing for ultrasonographic imaging modalities. . 26
4.2 (a) Conventional US. (b) Power Doppler. (c) conventional US and Elastrography were produced simultaneously. 30
4.3 (a) Conventional US. (b) Ground truth is obtained from expert radiologist. . . 30
4.4 Example of image inpainting in Elastography (a) Original image. (b) Mark segmentation is performed by region growing technique. (c) The green circle is replaced by nearby pixel applying linear interpolation. 31
4.5 Example of image inpainting in Power Doppler (a) Undesirable mark is shown as green rectangle. (b) Undesirable mark is replaced by inpainting. 31
4.6 Example of image inpainting in convention US is produced with Elastogrpahy simultaneously. (a) Undesirable mark is shown as green circle. (b) Undesirable mark is replaced by inpainting. 32
4.7 Example of image inpainting in Elastography (a) Undesirable mark is shown as green circle. (b) Undesirable mark is replaced by inpainting. 32
4.8 (a) Original size of conventional US image 996×812. (b) 25% of actual size 249×203. 33

4.9 (a) Original size of Power Doppler image 996×812. (b) 25% of actual size 249×203. 33

4.10 (a) Original size of Elastography image 639×870. (b) 25% of actual size 160×218. 34

4.11 (a) Original size of Elastography image 639×870. (b) 25% of actual size 160×218. 34

4.12 (a) convention US image. (b) Power Doppler image. (c) and (d) are conventional US and Elastography which are obtained simultaneously. 35

4.13 Image registration between conventional US and Power Doppler. 35

4.14 (a) Original Elastography. (b) The result of image registration between conventional US and Power Doppler. 36

4.15 Image registration between conventional US and Elastography. 36

4.16 (a) Original Elastography. (b) The result of image registration between conventional US and Elastography. 37

5.1 The process of developing an initial contour and proposed external force field of ACM for breast cancer detection utilizing the ultrasonic imaging modalities integration. 39

5.2 (a) Conventional US. (b) Edge map. (c) Dark gray mask. 41

5.3 Elastography image segmentation. 42

5.4 Example of (a) high stiffness segmentation and (b) common area of high stiffness area and dark region area 42

5.5 (a) Power Doppler image. (b) Binarized Power Doppler image. (c) Common area of vascular flows area and dark region area. 43

5.6 Binarized Power Doppler image after getting rid of outliers. 44

5.7 The results of Euclidean distance transform of (a) Edge Map, (b) Binarized Elastography, and (c) Binarized Power Doppler, are shown in (d)-(f) respectively. 45

5.8 Output of distance transform integration with the same weighting of D_E, D_{EG}, and D_{PD}. 46

5.9 Soft and hard(binary)intersection(a) U, (b) E, (c) D, (d) hard intersection of U, E, and D, (e) hard intersection of E, and D, and (f) soft intersection of U, E, and D. 51

5.10 a) E_D. (b)Binarized image. (c)E_F. (d) B_o 52

5.11 (a) D-image without the outliers (b) the convex hull B_D (c) contours $C_{F_1}(T_1)$, $C_{F_2}(T_1)$-obtained for $T = T_1$,$C_{F_1}(T_2)$ and $C_{F_1}(T_3)$ obtained for $T = T_2$ and $T = T_3$ (d) B_{o_1},B_{o_2} and B_{o_3} are the closest to B_D (e) $B_{o,2}$ passes the decision tree (f) $B_{init} = \gamma B_{o,2}$ 53

5.12 Decision tree is created by the CART algorithm [113] 54

5.13 Example of contour selection in automatic initialization. 54

5.14 External energy $g(x, y)$, proposed external force is created from center of outer boundary to outer boundary, E^1_{ext} is shown in blue, and E^2_{ext} is depicted in white. 55

7.1 (a) US image, (b) ground truth, (c) U_{edge}, (d) FM-initialization, (e) CoD initialization,(f) FFS-initialization, (g) PIG-initialization (h) QAI-initialization. Segmentation results: (i) FM/FRF (j), CoD/VFC, (k) FFS/VFC,(l)-PIG/VFC, (m) QAI/VFC 61

7.2 Force field: (a)FRF, (b) VFC, (c) ADF; snake evolution: (d)FRF, (e) VFC, (f) ADF; segmentation results: (g) FRF, (h) VFC, (i) ADF. 63

A.1 An example of IAC enhancement image. (a) Original image.; (b) Enhanced image. 88

A.2 The comparison of IAC segmentation between the GVF snake and the ADF snake focusing on weak edge leaking convergence. (a) GVF force field; (b) ADF force field; (c) GVF snake segmentation result; (d) ADF snake segmentation result; Both models use the same parameters for deformation, $\alpha = 0.1$, $\beta = 1$, $iteration = 60$. 89

A.3 A flowchart for segmentation and tracking of the ADF snake to find IACs in a 3D dataset. 90

A.4 An example IAC segmentation by ADF snake and its ground truth. (a) An original IAC image; (b) The bright contour depicts a result of an IAC segmentation by ADF snake ; (c) The apparent contour expresses a ground truth of an IAC. . 91

A.5 3D reconstruction of IAC from segmented cross-sections. (a) and (b) are the IACs at the right and left sides of the patient. 92

List of Tables

5.1 The evaluation of the size of an initial contour varying from 30-80% 50

7.1 Efficiency of initialization. FM vs. reference methods 61
7.2 FM vs. reference methods. Contour based measures 62
7.3 FM vs. reference methods. Region based measures 62
7.4 Impact of the radial force 63
7.5 Impact of the radial force. Contour based measures 64
7.6 Impact of the radial force. Region based measures 64
7.7 Efficiency of initialization for different combinations of the modalities 64
7.8 Contour based accuracy for different combinations of the modalities 65
7.9 Region based accuracy for different combinations of the modalities 65

A.1 Mean values for the analyzed indicators. 92

List of Abbreviations

2D	2-Dimension
3D	3-Dimension
ACM	Active contour model
ADF	Adaptive diffusion force active contour model
CAD	Computer aided diagnosis system
COD	Center of divergence
CT	Computed tomography
DICE	Dice index coefficient
FCM	Fuzzy C-means
FFS	Force field segmentation
FM	Fusion method
GGVF	Generalized gradient vector flow active contour model
GVF	Gradient vector flow
$\mathbf{H}_1$	Hausdorff distance
$\mathbf{H}_2$	Average Hausdorff distance
$\mathbf{H}_3$	Relative Hausdorff distance
HSV	Hue Saturation Value
HRCs	High resource contries
JAC	Jaccard similarity
LRCs	Limit-resource countries
MRI	Magnetic resonace imaging
PET	Positiron Emission Toography
PIG	Gradient vector flow
PPA	Phase Portrait Analysis

SEN	Sensitivity
TN	True negative
TP	True positive
RGB	Red Green Blue
QAI	Quasi-automatied initialization
ROI	Region of interest
US	Ultrasound
VFC	Vector field convolution

Chapter 1

Introduction

1.1 Overview of active contour model in breast cancer detection using ultrasonography image modalities

The annual check for breast cancer includes mammogram, and (if necessary) ultrasound examination of breast. Along with conventional US (US) imagery the modern US machines produce Elastography and Power Doppler images which in many cases improve the quality of the diagnosis [1]. Elastography distinguishes breast masses based on their stiffness and is used as a adjunct technique to help in discrimination between non-cancerous mass and breast cancer mass. Power Doppler is another non-invasive US modality which supplements a US. The Power Doppler images visualize the appearance and morphology of blood vessels associated with the mass. The Doppler analysis uses the fact that a non-cancerous mass has a little or no vascular flow whereas the breast cancer mass increases the blood flow in the vicinity of the tumor.

Along with the conventional US imagery, the modern US machines produce Elastography and Doppler images, which in many cases improve the quality of the diagnosis [2]. Elastography is used as an adjunct technique to help in discrimination between benign and malignant masses, based on their stiffness [3]. Power Doppler is another non-invasive US modality which supplements the conventional US. Doppler images visualize the appearance and morphology of blood vessels associated with the mass. The analysis uses the fact that a benign mass has little or no vascular flow, whereas a malignancy increases the blood flow in the vicinity of the tumor [4]. Since the Elastography and Power Doppler images are usually available in cases when cancer is suspected, we propose to use them, along with a conventional US image to improve the quality of automatic segmentation of breast tumors. In particular, we focus on the integration of the US, Elastography, and Power Doppler images in the framework of active contours (snakes).

The active contours are one of the most popular segmentation techniques applied to many image processing problems, originating from different applications. The most successful modifications of the active contours are the gradient vector flow (GVF) snakes [5], generalized gradient vector flow snakes (GGVF) [6], and multidirectional GGVF snakes [7], Vector Field convolution snakes (VFC) [8] and the recent Adaptive Diffusion Flow snakes (ADF) [9]. However, the accuracy and computational time of the above mentioned models depend on the initial location (seed snakes). Unfortunately, if the seeds are far from the boundary of the object, the snake can attach itself to false boundaries. On the other hand, the modern US/sharewave machines generate three types of above mentioned images. Each of them helps the radiologists to localize and classify the tumor i.e. the tumors are characterized by a low intensity of the gray level in the US image, high stiffness in the elasticity image and by an increased vascularity in the Doppler images. Therefore, we introduce a novel initialization method based on the fusion of the conventional US, elasticity and Doppler images. The proposed algorithm combines the images by means of the distance transform and a low intensity mask, and generates a suitable initial contour.

One of the popular ideas is analysis of the vector field generated by the GVF-type model. For instance applies force field segmentation (FFS) [10] to divide the image domain into disjointed regions representing the capture range of the external force field. However, the algorithm transforms the image segmentation problem into the vector field segmentation problem, which is difficult to solve if strong noise is present. Therefore, the idea to initialize the snakes at the centers of divergence (CoD)) [11] of the GVF-type vector field was introduced. The Poisson Inverse Gradient Vector Flow (PIG) [12] model has been proposed for automatic initialization of ACM. The model establishes the relationship between the external force field and the underlying external energy field via the solution of the corresponding Poisson equation. However, the model may suffer from incomplete isolines as well as from over segmentation. Quasi automatic initialization (QAI) [13, 14], the method employs the CoDs combined with a tracing procedure to create a ”skeleton” of the object, consisting of centers of strong and weak divergence. The initial snake is generated around the skeleton. However, the initialization is not entirely automatic. The algorithm still requires at least one manually generated point inside the object.

Moreover, in some cases the skeleton can evolve outside the boundary of the object. The initialization algorithms for the US images usually rely on gray levels and textures, to place the seed points inside the tumor. A few papers related to a specific medical image processing task use a typical position of a human organ in a US images. However, these models are image dependent and may not work if strong noise is present.

This paper proposes a new algorithm for automatic segmentation, uses not only the gray level/ texture which characterize the tumor but the corresponding Elasticity and Power Doppler images as well. The initialization procedure combines distance transforms generated using the binarized edge map, Elastography, and Power Doppler images. The techniques combined with a conventional thresholding makes it possible to locate the initial contour inside the tumor and close enough to the boundaries to ensure convergence of the ACM to the true boundaries. The paper also introduces a modification of the balloon type active contour based on a combination of an artificial (balloon) radial force and the gradient at actual boundary. Therefore, the main contribution of this paper is a new fusion based method to automatically initialize active contours in the US images of breast cancer. The proposed technique has been tested against three state-of-the-art models, namely, COD, FFS, PIG, and QAI for automatic initialization and VFC and ADF for external force evaluation.

1.2 Research Problem and Motivations

Breast cancer is the most common category of cancers in woman around the world. It is age diversity, especially the average age at diagnosis of breast cancer in limit-resource countries (LRCs) is approximately ten years younger than that in the developed world. Regular examination of breasts may prevent and help to cure at early stages when it is treatable. Therefore, a breast cancer screening modality being sensitive to dense breasts and suitable for general people in LRCs like Ultrasonography imaging modality, is strongly required.

The effective breast screening modality, Ultrasonography imaging and its adjunct modalities including conventional US, Elastography, and Power Doppler have been used in medical image processing for many years. Some researches use only conventional US while others prefer to US-based imaging modalities fusion. The combination of these images in feature analysis would give benefits as same as in the breast cancer diagnosis done by a radiologist. However, the combination made in the previous works are related the classification method to distinguish noncancer from cancer masses utilizing either the fusion of conventional US and Power Doppler or the combination of conventional US and Elastography. Unlike previous method, we proposed the new combination that are conventional US, Elastography, and Power Doppler in the domain of image segmentation. The research aims to detect breast cancer with high accuracy using US-based imaging modalities fusion.

Parametric active contour model is used as a main method for breast cancer mass segmentation. One of the crucial stage that affects its performance is initialization. Although, several researches have been proposed for an automatic initialization, their purpose are for multiple-object initialization. Normally, there is only one irregular hypoechoic mass presenting in conventional US. Therefore, the previous works may not be satisfied in breast cancer mass segmentation. We propose the method that is able to estimate only one initial contour located on the breast cancer mass correctly. Not only an automatic initialization is contributed in this research but also a new type of external energy of active contour model called radial force field. Refer to common external force, GVF and its extension forces extend the extra force in order to improve capture range from gradient of the edge map. The force is strong close to the gradient and become weaker when it is far from the edge map. In addition, when the edges are not so far from each other, the force often direct active contour model to converge to the wrong region of interest. The proposed force differs from previous force fields as the strength of the force is adaptive corresponding to the distance from the center of the mass to the masss boundary. The force is strong close to the masss center while weak near the boundary of the mass. The characters of the new force make active contour model robust to noise and improve iteration numbers to converge to the feature of interest.

1.3 Research Vision, Purpose and Objectives

The research vision is to improve performance of active contour model method in breast cancer segmentation.

The research purpose is to introduce an integration of ultrasonic imaging modalities including conventional US, Elastography and Power Doppler images. Their integration improves a performance of active contour model for initialization as well as an external force. Therefore, the results of breast cancer segmentation using active contour model have high accuracy.

The objectives of this research can be summarized as below.

1. The new approach of the integration of US-based images in image segmentation utilizing parametric active contour model in order to overcome drawbacks of the segmentation method.
2. Automatic initialization of parametric active contour model designed for only one initial contour.
3. Alignment of the integrated images to find the common area as suspicious region of a breast cancer mass.
4. Accurate segmentation of parametric active contour model utilizing new vector force field map.

1.4 Dissertation Scope

This research focuses on parametric active contour model applying on ultrasound imaging modalities including conventional US, Elastography and Power Doppler images.

1.5 Dissertation Outline

In this research, we developing the system for breast cancer segmentation using active contour model as a main method. The main purpose of this paper is to develop an automatic initialization and accurate segmentation of active contour model by extracting significant information from Ultrasonography based images including conventional US, Elastography, Power Doppler. There are two significant contributions in this research utilizing the US-based imaging modalities fusion; an automatic initialization and vector force field map called radial force field as an external energy for active contour model. Therefore, the description flow will be directed by the implementation of these contributions respectively. The overall processes of the proposed method is shown in Figure 1.1.

- US-based imaging modalities: the conventional US, Elastography, and Power Doppler was performed by Ultrasound scanner. Each breast mass dataset was first examined by conventional US and then by Elastography and Color Doppler respectively during the same session. The examination is conducted from expert radiologists.

- Materials: all obtained datasets require preprocessing techniques for getting rid of all artifacts from the diagnosis such as image inpainting, image registration.

- Edge map: due to the drawbacks of conventional US, it is not possible to utilize simple edge detection methods so fuzzy c-means algorithm is applied.

- High stiffness segmentation: first the image is converted from RGB color to HSV and then thresholding technique is applied in Hue channel to detect the light red and dark red interval representing the high stiffness area in Elastography image.

- Vascular flows segmentation: basically, in gray-scale regions, the intensity values of R, G, and B channels are almost same. Contrast with the color objects which have different intensity values in the three channels with big variance. Thus, color vascular flows are segmented based on the color objects properties.

- Dark gray region mask: Under the assumption that the dark gray area would likely to be the mass region and the light gray should represent for normal tissue. The dark gray regions are detected by applying Gaussian blur and following by thresholding technique to create binary image.

- Soft intersection using distance transform function: we utilize the integration of distance transform outputs, as a method to find common area among the US-based imaging modalities including edge map from conventional US, and the common areas between dark gray region in conventional US and high stiffness regions in Elastography as well as vascular flow regions in Power Doppler.

$$d_F(P) = w_P d_U(P) + w_E d_E(P) + w_D d_D(P).$$

- An initial contour: to find the boundaries of the common area from the integration of distance transform; first, it could be done by thresholding method to generate binary image. After that, the boundaries of all dark regions in binary image could be traced. The prospective boundary could be extracted by considering; it should has common area with the Power Doppler region; its center should be close to the center of Power Doppler region.

- Proposed external force filed: the internal energy is designed based on the initial contour from last process to create appropriate force based on coarse shape of a mass in order to improve wrong convergence and number of iteration for convergence of active contour model. The position of a snake parametrically by $v(s) = (x(s), y(s))$, we can write its energy function as

  $$E = \int_0^1 \lceil \frac{1}{2}(\alpha \cdot |v_s(s)|^2 + \beta \cdot |v_{ss}(s)|^2) + E_{ext}(v(s)) \rceil \, ds.$$

  The proposed external force $E_{ext}(v(s))$ is composted of,

  $$E_{ext}(v(s)) = E^1_{ext}(v(s)) + E^2_{ext}(v(s)).$$

  Where,

  $$E^1_{ext}(v(s)) = -|\nabla I(x, y)|^2.$$

  And proposed external force field $g(x, y)$,

  $$E^2_{ext}(v(s)) = g(x, y).$$

Examples and comparisons with three state-of-the-art automatic initialization methods (center of divergence COD, fast field segmentation-FFS, and Poisson inverse gradient-PIG) are demonstrated to present the advantages of the proposed method. Whereas, the accurate segmentation is evaluated by comparison of proposed method with a novel external energy, adaptive diffusion force active contour model (ADF). From the evaluation results show high accuracy of initialization as well as fast convergence to features of interest as shown in the last page.

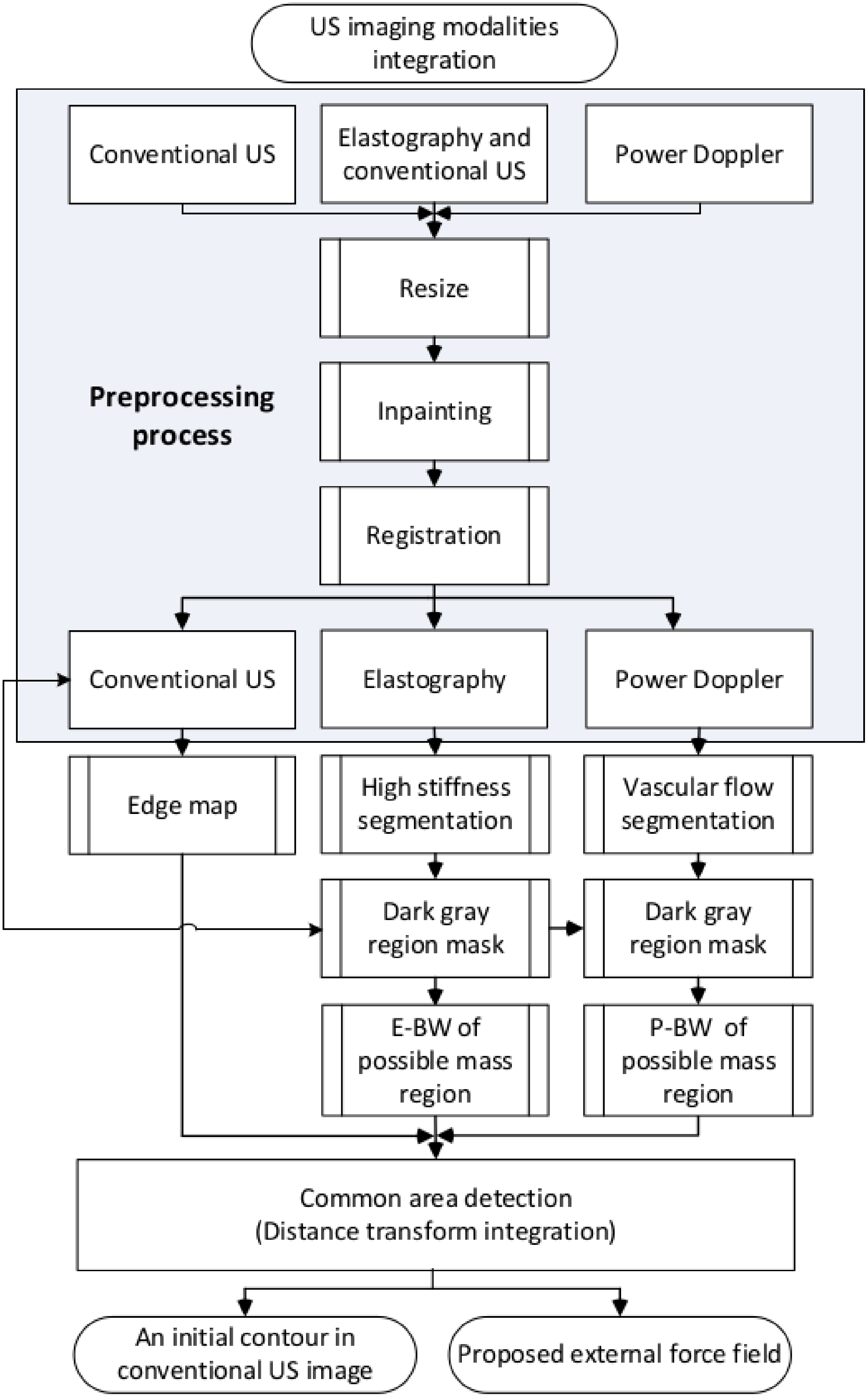

Figure 1.1: Over all process for improving performance of active contour model in breast cancer detection using ultrasonography image modalities

Chapter 2

Related work

2.1 Related Work

Segmentation of breast abnormalities has received considerable attention in the literature. An extensive review by Noble and Boukerroui [15] mentions that such segmentation can be treated as a general image processing problem, as well as include a priori information of ultrasound. The segmentation algorithms include numerous modifications of the conventional thresholding, neural networks (see a concise survey in [16]), watershed techniques [17], statistical methods [18, 19] , active contours (see extended surveys [20, 21], and a large list of references compiled in [22]), level set method (see recent surveys in [23, 24]), and graph-based segmentation refined by active contours [25]. Excellent results have been obtained combining a modified watershed model and all tissue classification for segmentation of 3D US images [26].

However, among these segmentation techniques, neural networks and other AI based methods require feature selection and training. Initial seeds are required for the watershed, and graph-based methods, as well as for the active contours and the level-set methods. Finally, an unsupervised Fuzzy C-means method (FCM) is a good alternative to techniques requiring prior information, training, and initial contours (see, a concise review in [27]). In particular [27] develops a new modification of the FCM based on Hausdorff distance and an adaptive selection of the neighbor region of each pixel for distance measurement and centroid updating. However, the classical disadvantages of the FCM are still a long computational time and relatively high sensitivity to the initial guess.

Apart from active contours, the proposed FM is potentially applicable to all of the above mentioned techniques, in particular to the watershed, level set initialization, and even to conventional or adaptive thresholding. We may conjecture that the FCM could also benefit from the FM since basically, the initial contour provides additional information about a possible location of the tumor. However, such combinations lie out of the scope of this paper. Our focus is the initial seeds for the active contours.

Let us review some ideas developed specifically for the active contours. One of the most popular techniques is analysis of the vector field generated by the GVF-type model [5]. For instance, [10] applies FFS to divide the image domain into disjointed regions representing the capture range of the external force field. The snakes can be individually initialized within each of the enclosures and moved to the targeted object boundary within it, avoiding being attracted by other objects. However, the algorithm transforms an image segmentation problem into a vector field segmentation problem, which is difficult to solve if strong noise is present.

The idea to initialize the snakes at the CoD of the GVF-type vector field was first mentioned in [28]. Further, Ge and Tan [11] define the CoD by analyzing relative directions of the vector field in a sliding 2x2 window (a generalization to larger windows is not available). He et al. [29] uses Phase Portrait Analysis (PPA) [30] to detect the critical points of the vector field and a rule that ”the initial contours should be set to contain all of the node points in the object area and none of the others”. Although PPA has been used in a variety of image processing applications, e.g. [30–35], the standard PPA classifier based on ”if then” rules often can not be adapted to the case of snake initializations characterized by irregular nodes corrupted by noise.

The similarity of the GGVF and the Navier-Stokes equations makes it possible to use the analogy of a flow through a porous medium. Consequently, [36] treats the initial snakes as sources of flow, emitting normal unit vectors into the image domain. The authors also noticed critical points of the flow and proposed to merge multi-snakes initialized around those points for segmentation of the MRI images of lungs.

A competing idea is placing the seed points uniformly or randomly over the entire image, evolving them from each seed point, and analyzing the resulting configuration [37]. However, the required classifier to validate the final configuration must be trained, which makes the model image-dependent.

A partial solution to the problem is the above mentioned QAI method by Tauber et al [13, 14]. The method employs the CoDs combined with a tracing procedure to create a ”skeleton” of the object, consisting of centers of strong and weak divergence. The centers of weak divergence are the points where the vectors of the GVF diverge in one (either horizontal or vertical) direction. The centers of strong divergence feature both horizontal and vertical divergences. The initial snake is generated around the skeleton. However, the initialization is not entirely automatic. The algorithm still requires at least one manually generated point inside the object. Moreover, in some cases the skeleton can evolve outside the boundary of the object.

The above mentioned PIG model [12] establishes the relationship between the external force field and the underlying external energy field via the solution of the corresponding Poisson equation. The model has been applied to 2D and 3D cases for a variety of medical images. The isoline of the minimum energy is selected as the initial contour. However, the model may suffer from incomplete isolines, as well as from over segmentation.

An automatic initialization method has been proposed in [38] for PET images of the liver. The candidate contours are generated by Canny edge detection and subsequently classified by a genetic algorithm. The algorithm has been applied to segmentation of face contours in video files [39]. A similar idea was introduced in [40] for detection of the synovial boundaries in US images. However, the proposed initial snakes selected from the edge map are not robust and may not be applicable to multiple objects.

The idea of trial snakes (TS), combined with PPA, was applied to US images of breast cancer in [41]. The PPA makes it possible to detect the centers of convergence and divergence, as well as the attracting and repelling nodes. The algorithm differentiates between the internal and external seeds by running multiple TS from the critical points and checking their intersections with the boundary of the image. The most serious drawback of TS is that they require a considerable amount of computational time.

The initialization algorithms for the US images often rely on gray levels and textures, to place the seed points inside the tumor [42–44]. Saliency and feature maps have been proposed in [45]. [46] introduces a special vector field to hybridize the GVF and the texture. A Chan-Vese type model is proposed in [47]. A few papers related to a specific medical image processing task use the typical position of a human organ in the US images (see, for instance, [48]). However, these models are image dependent and may not work if strong noise is present.

Therefore, this paper proposes a new fast algorithm for automatic initialization, which combines the conventional grayscale US image with the corresponding elasticity and Doppler images. The technique makes it possible to locate the initial contour inside the tumor, close enough to the true boundaries to ensure convergence of the active contour. The paper also introduces a modification of the balloon type active contour, based on a combination of the radial force derived from the fusion image and the GVF-type force.

Chapter 3

Background

3.1 Introduction

Breast cancer is ranked as the most common disease in woman around the world. Especially the patients is increasing dramatically in developing countries. Breast cancer is treatable when it is examined at early stages. Although regular examination of breasts may prevent and help to cure, almost the cases of breast cancers in developing countries or low resource countries (LRCs) are detected in the advance stages. It is likely not possible for the treatment. The examination of adequate breast screening techniques is not considered only for the cost but also the rate of abnormality detection in age diversity because breast cancer patients include adults and teenagers both. Ultrasonography imaging modality, is sensitivity and likely to improve screening accuracy in dense breast [49, 50]. It is more affordable, portable, comfortable and easy accessibility. In addition, there are various kinds of adjunct US-based imaging modalities provided for improving accuracy of breast cancer diagnosis such as Elastography and Color Doppler.

The state-of-the-art method for feature segmentation especially in medical image modalities, active contour model or snake has been known for decades. Numerous researches have been conducted to improve the drawbacks of traditional snake such as concavity convergence, noise robustness, weak edge preserving, and initialization insensitivity [5], [8], and [51]. However, an initialization as an important step that affects the ultimate active contour model performance has not been investigated dramatically. Specificity related to US image modality, there are only the semi-automatic initialization in conventional US [13], and the application applied to 3D

Elastography for liver segmentation [52]. However, in realistic diagnosis especially in LRCs the 2D Ultrasonography imaging modalities are more effective.

The main purpose of this paper is to improve performance of parametric ACM by integrating significant information from US, Elastography, and Power Doppler to estimate a location for setting an initial contour as well as developing a suitable external force field be able to drive ACM passing speckle noises. Unlike previous methods are proposed for multi-object segmentation [11], [10], and [12]. We introduce the method estimating only one initial contour because generally there is only one suspicious mass in the conventional US image. It is very challenging due to the drawbacks of conventional US including sparkle noise, shadows, and non-uniform in contrast of certain structure.

3.2 Applying Ultrasonography imaging modalities in breast cancer screening

World Health Organization reports the breast cancers as the most common category of cancers in women both in the developed and the developing world. In addition, the cases of breast cancers in developing countries are increasing due to the increase in life expectancy, urbanization, and western lifestyles [53]. Breast cancer is defined as a cancer that develops in the interval between routine screening. Hence, regular examination of breasts may prevent and help to cure because breast cancers are detectable at early stages when they are treatable. Therefore, an appropriate breast screening modality is strongly required. Although, there are many non-invasive imaging techniques existing to diagnose breast cancer such as computed tomography (CT), magnetic resonance imaging (MRI), the most common methods have been used are mammography and ultrasound. Considering to the cost-effective and practical methodology, mammography may not be appropriate in LRCs. Although it has proved to be effective and worked well in high-resource countries (HRCs), it is not a feasible option as a screening modality for the common population in LRCs [54]. Moreover, the most breast cancer patients are detected in relatively advance stage when a treatment is less possible to be successful due to the limited breast cancer awareness as well as weak health systems [55].

The examination of adequate breast screening techniques is not considered only for the cost but also the rate of abnormality detection in age diversity because breast cancer patients include adults and teenagers both. Especially, the average age at diagnosis of breast cancer in LRCs is approximately ten years younger than that in the developed world [56]. Normally, screening sensitivity is mostly based on breast density which relate to age groups. The woman is younger than 50 has dense breast (the proportion of breast value) and since, mammography is less effective in woman below the age of fifty. Therefore, it has been considered relatively unsatisfactory in young woman. Hence, recall of the disadvantages of mammography technique which is expensive, requires skilled manpower and stringent quality control, is on the whole complex screening test, and is less sensitivity in dense breast screening, it may not be an appropriate technique for breast cancer screening test in LRCs. In contrast with, Ultrasonography imaging modality (US), is considered sensitivity, and likely to improve screening accuracy in dense breast [49], [50], and [57]. Moreover, it is more affordable, portable, more comfortable compared to mammography as well as easy accessibility. Therefore, the ultrasound is most likely be appropriate for breast cancer screening modality in LRCs [54] and [55]. Thus, the research focusing on ultrasound imaging modality in the domain of computer aided diagnosis system may help in breast cancer control and improve the survival rates especially in LRCs.

3.3 The integration of Ultrasonography imaging modalities in improving sensitivity and specificity

Traditionally, the assessment processes recommended for symptomatic woman are physical assessment (palpation), screening and diagnosis (imaging modalities), and fine-needle aspiration cytology (biopsy) consequently. As a median process, the effective imaging modality, a supporting tool for radiologist to acquire accurate diagnosis is needed in order to decrease the unnecessary biopsy rate. Although US image provides numerous benefits as mention in the previous section, the quality of US image may not be satisfied according to speckle noise, shadows, and low or non-uniformity in contrast of certain structure. Therefore, using only US image might cause the increase in false-positive diagnosis. Consequently, the supplement imaging modalities in US using as adjunct to conventional US are invented in the purpose of improving diagnosis accuracy which are Ultrasonographic Elastography and Power Doppler Ultrasonography.

3.3.1 Conventional Ultrasound

Ultrasonographic Elastography (Elastography)

Elastography is a non-invasive medical imaging modality that distinguishes breast masses based on their stiffness. The visualization of Elastography method is similar to the palpation assessment that evaluates the hardness of a breast mass. Consequently, it is used as a adjunct technique to help in discrimination of benign and malignant breast mass especially when the mass is non-palpable [58]. Referring to strain pattern scoring [59], score 1, completely blue color mass refers to a soft and loose structure. Score 2, blue and green color mass refers to a soft-rigid internal structure. Score 3, red and dark red in the center of the mass and green in periphery refers to harder in its center and softer on the outside. Score 4, completely red and dark red color mass refers to whole mass being hard and tight. Finally, a score 5, red and dark red color covering the mass and the surrounding tissue refers to hard structure in both mass and its surrounding area. The color bar that represent the stiffness of a breast mass is showing in Figure 3.1. According to the mass characteristic, benign lesions tend to be harder than normal breast tissue but significant softer than malignant lesions. The score 1, 2, and 3 represent benign features whereas the masses scoring 4 and 5 are interpreted as malignant. The US machine displays a color Elastography image as follows:
Score 1: blue color indicates soft and loose structures.
Score 2: a combination of blue and green indicates soft-rigid structures.
Score 3: red and dark red at the center of the mass and green at the periphery indicates a hard to soft mass.
Score 4: red and dark red indicates a hard and tight mass.
Score 5: red and dark red covering the mass and the surrounding tissue refers to a hard expanding mass. Scores 1, 2, and 3 represent benign features, whereas masses scoring 4 and 5 are likely to be malignant.

In order to improve sensitivity (discrimination of benign and malignant) as well as specificity (a necessity of biopsy), the combining of conventional US and Elastography for breast cancer diagnosis is required and it has shown satisfied results [58], [60], and [61].

Figure 3.1: Color bar shows stiffness of a breast mass in Elastography.

Color Doppler or Power Doppler Ultrasonography (Power Doppler)

Power Doppler is also a non-invasive image modality supplement to conventional US. It can support to visualize the appearance and morphology of blood vessels associate with the breast mass. The Power Doppler is under the assumption that neoangiogenesis within a malignant mass may enable differentiation from benign mass by considering the demonstration of vascular flow. Normally, a benign mass has a little or no appearance of vascular flow. The advantages of Power Doppler are high sensitivity to slow flow, no angle dependency, and no aliasing [62] and [63]. Therefore, it is wildly used as an adjunct image modality for beast cancer diagnosis in distinguishing benign from malignant mass and the optimistic results have shown in [62] and [64].

The integration of conventional US, Elastography, and Power Doppler

Basically, evaluation of breast cancer in conventional US considering to mass shape, boundaries, location, echogenicity, appearance of acoustic strengthening, and calcification content which is not sufficient enough to reduce false-positive diagnosis. According to the benefits of the supplement US imaging modalities; Elastography and Power Doppler, the combination of them improve the accuracy of radiologists in terms of sensitivity and specificity [4]. From fig. 3.2, a mass which appears as dark region in conventional US, and presents as red and dark red shed covering a whole part of the dark area (hard tissue) in Elastography, and also emerges of a number of vascular flows at the dark area in Power Doppler should be classified as a malignant mass.

Integration of the imaging modalities in clinical practice

The efficiency of combined US, Doppler, and elasticity imaging in diagnosing breast malignancy is still controversial. For instance, [65] reports that “using the Doppler image alone has little value in differentiating between malignant and benign breast lesions”. The research conducted by [66] concludes that Doppler imaging does not contribute to categorization of

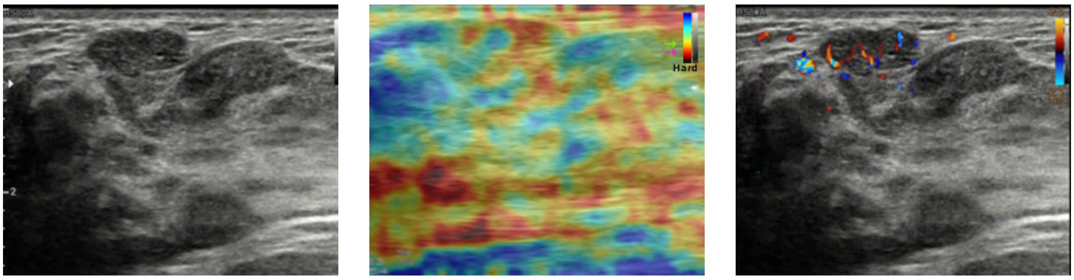

(a) (b) (c)

Figure 3.2: US images in a patient at Thammasat university hospital show high suspicious of malignant mass. (a) Conventional US shows an irregular hypoechoic mass. (b) Elastography shows the entire mass as red and dark red. (c) Power Doppler shows increased vascularity.

solid breast masses. However, there is growing evidence that analysis of a combination of images improves the characterization of breast lesions. [67] reports that sensitivity/specificity was 96%/68% for US, 100%/40% for US and mammography, and 96%/80% for the combined mode, including Doppler. [4] characterizes the results obtained from 5 readers by the area under the receiver operated characteristic curve A_z as follows: "the A_z of the US mode, elastography, and Doppler US (average, 0.844; range, 0.797-0.876) was greater than that of the US mode alone (average, 0.771; range, 0.738-0.798) for all readers". [68] reports "the specificity of making the decision for biopsy increased from 6.5% to 38.7% when US was combined with color Doppler and elasticity without a statistically significant change in sensitivity". [69] shows that a combined use of US, elasiticity, and color Doppler achieved an NPV of 95% "thus allowing sparing of unnecessary invasive diagnostic procedures". In summary, there is enough evidence that a combination of the conventional US, elastography, and Doppler images improves the accuracy of diagnosis. Therefore, the above imaging modalities will be increasingly used in clinical conditions to allow for computerized segmentation and classification of tumors.

3.3.2 The integration of Ultrasonography imaging modalities in medical image processing

One of the targets for medical image processing is to develop computer aided diagnosis system (CAD) which is the software invented to assist physicians and radiologists in examination of medical images. The processes in CAD system are started from image enhancement and restoration, registration and fusion of multi-modality images, segmentation of feature interest, classification of image feature, quantitative measurement of image features and interpretation of the measurement, and finally, the development of integrated systems for the clinical sector [70]. Based on the advantages of combining conventional US, Elastography, and Power doppler in breast cancer diagnosis, it could be applied in medical image processing. Most of researches conducted in the US images fusion is in the classification of image feature process for distinguishing benign from malignant masses. The combination could be either conventional US and Elastography [71] and [72], or conventional US and Power Doppler [73], [74], [75], and [76]. Only one research for segmentation was conducted in 3D Elastography using active contour model [52]. However, there is no full combination of images (conventional US, Elastography, and Doppler image modalities).

3.3.3 Segmentation of breast cancer

According to the benefits of the US-based imaging modalities fusion for differentiating the breast cancer mass (malignant) from normal lesion (benign), it make optimistic improvement of fault-positive diagnosis in terms of sensitivity and specificity. Although, the images were applied widely for classification, it was only few researches using them for segmentation. Especially, there is none in the combination of the all three images. Therefore, we originally propose the Ultrasonography imaging modalities fusion for malignant mass segmentation using active contour model. By extracting the significant image features from each image to identify the most likely to be malignant mass including the dark region in conventional US, the red and dark red shed in Elastograpy, and the emerging area of vascular flow in Power Doppler. The common of all three areas should represent the most possible location for malignant mass.

3.4 Active contour Model

The energy driving algorithm, active contour models or snakes have been used dramatically in image segmentation, feature recovery, as well as tracking. There are two main types of snakes: parametric snakes [5, 77–79] and geometrical [80–83] ACMs. This research focuses on parametric snakes working based on parameterized contour and then the snake deforms by evaluating its positions on the predetermined spline contour points until it reaches the region of interest (ROI) where is the equilibrium position. The traditional snake [84] composes of two energy term to perform energy minimization including internal and external energy forces. The position of a snake parametrically by $v(s) = (x(s), y(s))$, we can write its energy function as

$$E = \int_0^1 \lceil \frac{1}{2}(\alpha \cdot |v_s(s)|^2 + \beta \cdot |v_{ss}(s)|^2) + g(v(s)) \rceil \, ds.$$

where the subscripts denote partial derivatives, α and β are weighting parameters to control the snake's tension and rigidity and $g(v(s))$ is the external force.

3.4.1 An automatic initialization of parametric active contour model

The critical problem of active contour model, setting of the initial contour is started from assigning by the user. The popular way to initiate a contour is creating simple shape such as rectangle and circle either inside or outside the ROI. This method is uncomplicated but it may cause a big number of iterations from starting point to the desired boundary. It also could make wrong segmentation, when there are more than one objects and\or noisy image. According to the static force field map, ts make these drawbacks be challenge. The sensitivity of the direction of force fields could cause wrong segmentation when an initial contour is placed in an inappropriate location. Therefore, the research focusing in an automatic initialization has been increasingly investigated. The first attempt method [85] relies on the distant end points given by a user. After the successful contribution of GVF, there are dramatic interest in developing an automatic initialization methods related to the gradient vector flow. For example, semi-algorithm [29] analyzed the critical points in the force field for estimating the position for initial contour. Contrast to the previous works, targeting for multiple objects, the multiple automatic initialization [11] utilized the center of divergence of the force field as appropriate locations to place the small initial contours. Li and others [10] proposed automatic initialization by inventing external force field and solved the complex shape boundaries by splitting method. The same research team of VFC snake [12] invented the method that can specify the number of the object for automatic initialization using Poisson inverse gradient analysis. Specificity, previous works related to US image modality, the semi-automatic initialization in conventional US [13], requiring a user to select a point in the ROI, the method estimated the position to set up an initial curve by evaluating strong and weak divergence. Another one applied to 3D Elastography for liver segmentation [52], the coarse-to-fine method used Gaussian pyramid to find an appropriate position for curve initialization.

One of the purposes of this paper is to develop an automatic initialization of active contour model by extracting significant information from the US images to find the appropriate position for locating an initial contour of snake based on static map deformation. It is challenging due to the drawbacks of conventional US including sparkle noise, shadows, non-uniform in contrast of certain structure. Moreover, beast screening in conventional US image modality normally presents more than one dark region which might be masses, shadows, cysts, and\or muscles. In very noisy images, it is even more difficult to distinguish a mass from noise by an expert. That's why, Tauber's work [13] required a user to select a point in the area of segmentation target. In addition, generally there is only one suspicious mass in the conventional US image. Thus, the automatic initialization methods for multiple objects [11] [10] would not be much appropriate to be applied in breast cancer detection. Hence, we originally propose an automatic initialization for parametric active contour model base on static-map of vector flow analysis to find only one specific region representing a malignant mass by extracting useful information from the fusion of Ultrasonography imaging modalities including conventional US, Elastography, and Power Doppler. Nevertheless, our propose method is specific to parametric snake which evaluate its position base on vector flow thus the proposed method may not be benefit to geometric snake.

3.4.2 An internal force of ACM.

From above equation, the combination of two forces leads ACM to desired boundaries including internal and external-force. The internal-force is calculated from the position of contour in each iteration as follow,

$$E_{int} = (\alpha(s)|v_s(s)|^2 + \beta(s)|v_{ss}(s)|^2)/2.$$

The energy is composed of a first-order (elastic) term to control by $\alpha(s)$ for energy weighing and a second-order (bended) term controlled by $\beta(s)$.

To improve performance of ACM, many researches have been utilized to improve the external of ACM to overcome the its disadvantages including deep and narrow concavity, weak edge leaking, capture range and noise robustness.

3.4.3 An external force of ACM.

The ACM is attracted to the desired boundary from a fairly large distance away because of the internal energy term. This type of convergence is rather common for ACM. If part of ACM finds a low-energy image feature, the spline function will pull neighboring parts of the ACM toward a possible continuation of the feature which called a good local minimum. The simplest useful image functional for external force to guild ACM to local minimum, is the edge energy function defined as,

$$E_{ext1} = -(G_\sigma * \nabla^2 I)^2$$

Although the edge energy is satisfied for energy minimizing, it is poor for far large distance of ACM development. It causes disadvantages of ACM as following;

- Small capture range.
- Deep and narrow concavity.
- Weak edge leaking.
- Noise robustness.

A number of research groups have generalized [86] via replacing the standard external force by the sum of other forces generated from the image and/or the contour [5, 6, 87, 88]. Instead of a standard energy minimization problem, the solution of the ACM is formulated as a force balance equation. Different external forces have been proposed to improve the performance of ACM. The external forces can be generally classified as dynamic forces and static forces [5].

The dynamic forces are those that depend on the ACM and, as a result, change as the ACM deforms. The static forces are those that are calculated from the image, and remain unchanged as the ACM deforms. The static forces can be further classified based on the force sources. Edge-based static forces are calculated from the image edges, whereas region-based static forces are computed using the region intensity and/or texture information [89]. The pressure force, also known as the inflation force, used in balloon models is an useful dynamic force that pushes the ACM either outward (inflation) or inward (deflation) [86, 87, 90–92]. Although the pressure force can avoid spurious edges, the pressure force causes leakage problem when there are significant gaps in the edges. Another limitation of the ACM using a pressure force is that it must be initialized either inside or outside the targeted object.

The most successful modifications of the active contours are Gradient Vector Flow (GVF) snakes [5], the Generalized Gradient Vector Flow snakes (GGVF) [6], multidirectional GGVF snakes [7] and the non-linear diffusion model [93]. Recent GVF-type models are Normal Gradient Vector Flow [94], Infinity Laplacian [95], Harmonic Gradient Vector Flow [96], Convolution Vector Flow [8], Dynamic Directional Gradient Vector Flow [97], Adaptive Diffusion Flow [9], and Multi Feature Gradient Vector Flow [98].

Numerous researches have been conducted to improve the drawbacks of traditional snake such as concavity convergence, noise robustness, weak edge preserving, and initialization insensitivity. The gradient vector flow or GVF snake [5] is one of the most successful algorithms to improve capture rank of snakes and then the massive of its extension are lunched in the purpose of overcoming the snake's drawbacks for example, the vector field convolution (VFC) [8] succeeding in handing the superior noise, the integration of GVF and the prior directional information provided by user to guide the snake's deformation in desired direction [99], the adaptive diffusion flow active contour model (ADF) [51] overcoming all of the problems, etc. The force field applied in snake's deformation is categorized into two type; static map-the force field map has been provided before snake starts evaluating such as GVF, VFC, and ADF; and dynamic map-the force field is modified and\or developed while snake deforming for instant [100]. Although, many drawbacks of snake have been mentioned and solved, an important disadvantage of snake is still being concerned, the automatic initialization of snake.

Not only an automatic initialization is contributed in this research but also a new type of external energy of active contour model. Refer to common external force, GVF and its extension forces extend the extra force in order to improve capture range from gradient of the edge map. The force is strong close to the gradient and become weaker when it is far from the edge map. In addition, when the edges are not so far from each other, the force often direct active contour model to converge to the wrong region of interest. The proposed force differs from previous force fields as the strength of the force is adaptive corresponding to the distance from the center of the mass to the masss boundary. The force is strong close to the masss center while weak near the boundary of the mass. The characters of the new force make active contour model robust to noise and improve iteration numbers to converge to the feature of interest.

Chapter 4

Ultrasonographic imaging modalities preprocessing and registration

Since all datasets of ultrasonic images including conventional US, Elastography, and Power Doppler were obtained from scanning machine via radiologist. The images were investigated for breast cancer diagnosis by radiologist which contain undesirable masks as well as different alignment of ROI due to obtaining in different time. Therefore, methods for image processing such as image inpainting, image transformation, and image registration are needed. The pipe line of image preprocessing and image registration is shown in Figure 4.1.

4.1 Materials

4.1.1 Sequence of ultrasonic imaging modalities

The conventional US, Elastography, and Power Doppler was performed by Ultrasound scanner Sumsung RS80A, 2D mode, Power Doppler(PD), and ElastoScan Mode with linear array L3-12A probe.The 90-dataset are obtained by expert radiologists who have experience for more than three years for breast cancer diagnosis and obtaining the image modalites at Radiology department, Thammasat university hospital, Pathumthani, Thailand. Each breast mass dataset was first examined by conventional US and then by Elastography and Color Doppler respectively during the same session. Example of ultrasonographic imaging modalities dataset that is obtained from the scanner is shown in Figure 4.2.

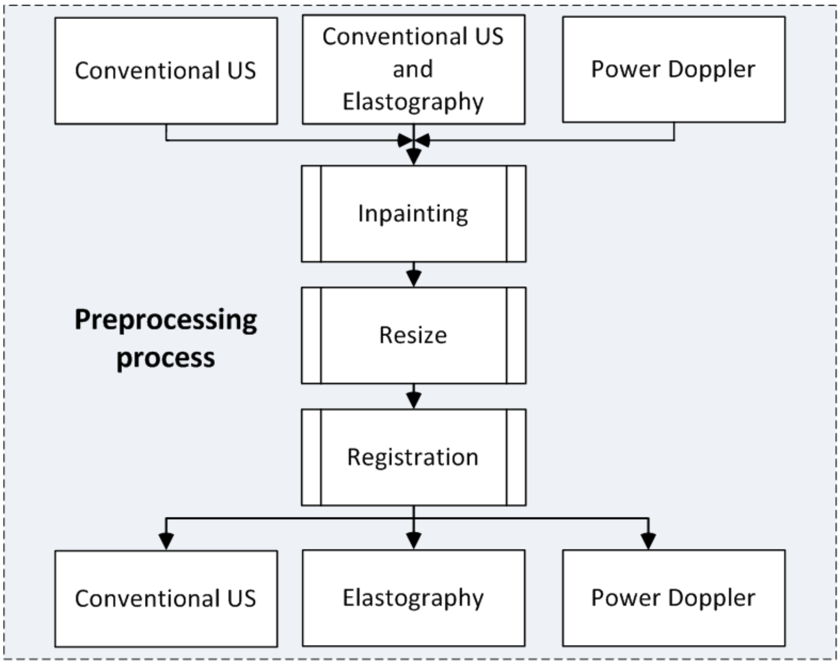

Figure 4.1: The process of image preprocessing for ultrasonographic imaging modalities.

4.1.2 Ground truth of conventional US

Since conventional US is used as information for external force of ACM for breast cancer segmentation. Therefore, evaluation of FM is done by comparing the segmented results from FM, FFS, COD, and PIG with ground truth form expert radiologist who has experience for breast cancer diagnosis for more than five years at Radiology department, Thammasat university hospital, Pathumthani, Thailand. An example of ground truth is shown in Figure 4.3.

4.2 Preprocessing process

Since Power Doppler and Elastography were obtained from scanning machine while diagnosis processes. Therefore, the images contain undesirable masks so that image inpainting and image transformation are required to get rid of undesirable marks and transform the images into suitable size for reducing time in image processing techniques.

4.2.1 Image inpainting

According to processes for breast cancer diagnosis performing by radiologists, Power Doppler and Elastography images have some undesirable marks which have to remove shown in Figure 4.5 to Figure 4.7 (a). Therefore image inpainting or image interpolation is required. In this work, a simple region-based image segmentation, region growing technique [101] is applied first for undesirable features segmentation following by linear interpolation [102] for filling texture using nearby texture information. Example process for image inpainting in Elastography is shown in Figure 4.4. The results of the images after image inpainting are shown in Figure 4.5 to Figure 4.7 (b).

4.2.2 Image resize

The actual size of ultrasonic imaging modalities obtaining from the machine is quite huge (996×812). Therefore, all datasets are resized to be 25% of their actual size which is performed by effective image resize technique [103] still preserving all important features. Example of original and resized images for conventional US, Power Doppler, and Elastography are shown in Figure 4.8 to Figure 4.11 respectively.

4.3 Image registration

Although, breast mass dataset was first examined by conventional US and then by Elastography and Power Doppler respectively during the same session, it causes slightly different position of a mass in each image shown in Figure 4.12. Hence, thin plate spline method [104] is conducted for manual registration between convention US, Power Doppler, and Elastography images. According to the images produced from the scanner provide corresponding features in conventional US, Power Dopplwer, and conventional US in Elastography mode which could be used for image registration. Therefore, the conventional US image is used as a main corresponding features for manual registration with Power Doppler and Elastography.

The process of image registration using thin plate splines, given two images to deform an image so it matches another one. The manual process is done by user providing set of corresponding points on the two images.

4.3.1 Thin plates spline

There are quite a few techniques out there that provides a smooth interpolation between a set of control points. Thin plate splines is one of such techniques. It interpolates a surface that passes through each control point. As set of three points will thus generate a flat plane. The control points are as position constraints on a bending surface. The ideal surface is on that bends the least. The least bent surface is given by the following equation,

$$f(x,y) = a_1 + a_2 x + a_3 y + \sum_{i=1}^{n} w_i U(|P_i - (x,y)|).$$

The first three terms correspond to the linear part which defines a flat plane that best matches all control points (this can be seen as a least square fitting). The last term corresponds to the bending forces provides by n control points. There is a coefficient w_i for each control point. Also $|P_i - (x,y)|$ is the distance between the control points P_i and a position (x,y). This distance is used in the function U defined by $U(r) = r^2 log\, r$.

The unknown are the coefficients a_1, a_2, a_3, and w_i for every control point. All w_i forms the vector W. These unknowns are defined by,

$$L^{-1}V = (W|a_1 a_2 a_3)^T.$$

What is known are the control point positions (x_i, y_i) of all points P_i and their heights v_i. Where the control point position is defined as,

$$P = \begin{bmatrix} 1 & x_1 & y_1 \\ 1 & x_2 & y_2 \\ \cdots & & \\ 1 & x_n & y_n \end{bmatrix}.$$

And the control point heights, padded with 0s,

$$Y = \begin{bmatrix} v_1 \\ v_2 \\ \cdots \\ v_2 \\ 0 \\ 0 \\ 0 \end{bmatrix}.$$

Matrix K is definded for evaluating the function $U(r_{ij})$ where r_{ij} is the distance between two control points, $r_{ij} = |P_i - P_j|$,

$$K = \begin{bmatrix} U(r_{11}) & U(r_{12}) & \dots \\ U(r_{21}) & U(r_{22}) & \dots \\ \dots & \dots & U(r_{nn}) \end{bmatrix}.$$

The matrix L mentioned earlier is composed with the matrix K on its top-left corner, with the matrix P on its right side, with the matrix P^T on its bottom side, and with zeros on it bottom-right corner,

$$L = \begin{bmatrix} K & P \\ P^T & 0 \end{bmatrix}.$$

To find the unknown coefficients, that is the matrix $(W|a_1\ a_2\ a_3)$, we can either find the inverse L^{-1}, or solve $L(W|a_1\ a_2\ a_3) = Y$ which is a linear system. Since L is by definition symmetric, the last system can be easily solved with for instance a LU decomposition.

Once $(W|a_1\ a_2\ a_3)$ is computed, then substitute back and find the height $v = f(x, y)$ for any point (x, y).

In this research focuses on a 2D point, but the method can be extended to N-D by adding more term a_i and by using a larger vector P. The result would still be the interpolation of height of the hypersurface, that means a 1D variable.

4.3.2 Image registration between conventional US and Power Doppler

The flow of conventional US and Power Doppler is shown in Figure 4.13. The results of the manual registration are shown in Figure 4.14.

4.3.3 Image registration between conventional US and Elastography

The flow of conventional US and conventional US which was produced simultaneously with Elastography is shown in Figure 4.15. The results of the manual registration are shown in Figure 4.16.

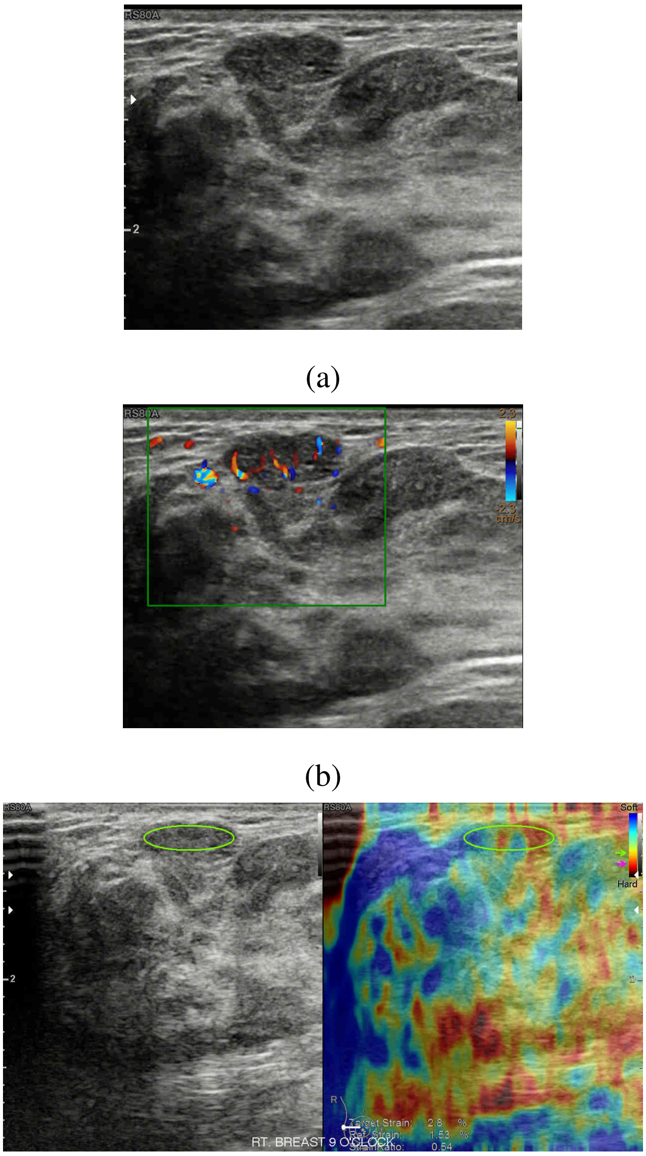

(a)

(b)

(c)

Figure 4.2: (a) Conventional US. (b) Power Doppler. (c) conventional US and Elastrogrpahy were produced simultaneously.

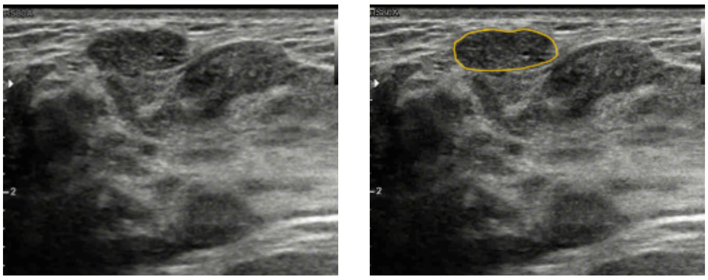

(a) (b)

Figure 4.3: (a) Conventional US. (b) Ground truth is obtained from expert radiologist.

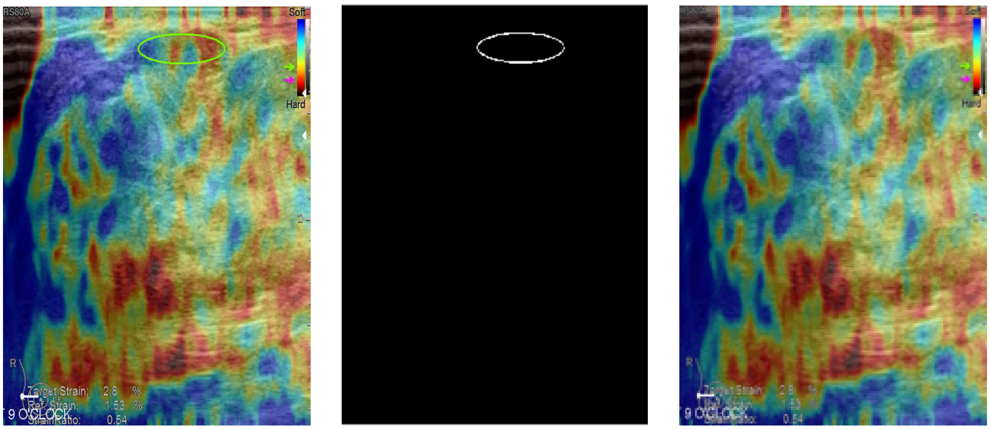

(a) (b)

Figure 4.4: Example of image inpainting in Elastography (a) Original image. (b) Mark segmentation is performed by region growing technique. (c) The green circle is replaced by nearby pixel applying linear interpolation.

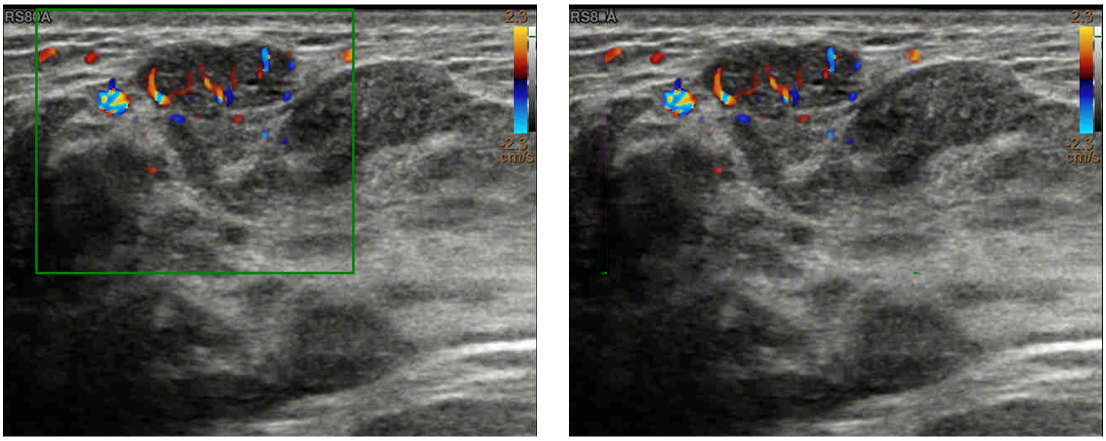

(a) (b)

Figure 4.5: Example of image inpainting in Power Doppler (a) Undesirable mark is shown as green rectangle. (b) Undesirable mark is replaced by inpainting.

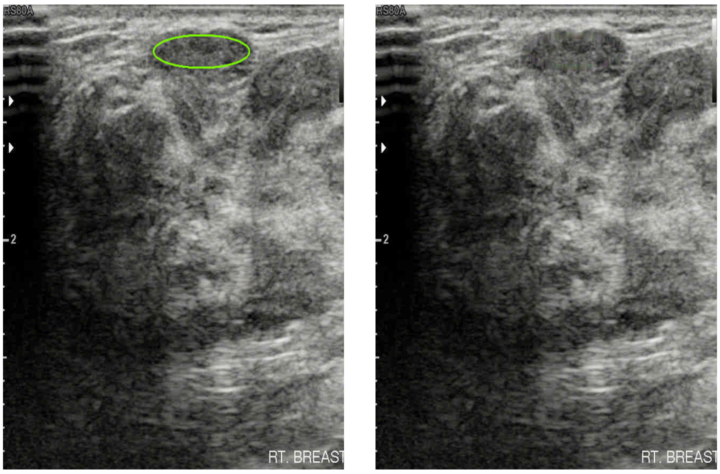

(a) (b)

Figure 4.6: Example of image inpainting in convention US is produced with Elastogrpahy simultaneously. (a) Undesirable mark is shown as green circle. (b) Undesirable mark is replaced by inpainting.

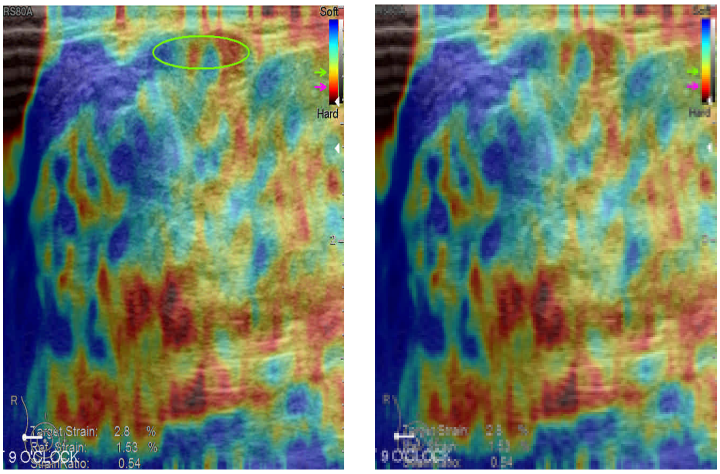

(a) (b)

Figure 4.7: Example of image inpainting in Elastography (a) Undesirable mark is shown as green circle. (b) Undesirable mark is replaced by inpainting.

203.

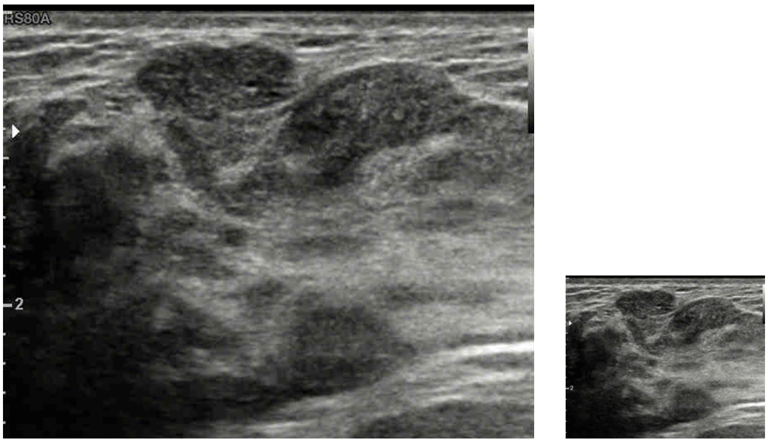

(a) (b)

Figure 4.8: (a) Original size of conventional US image 996×812. (b) 25% of actual size 249×203.

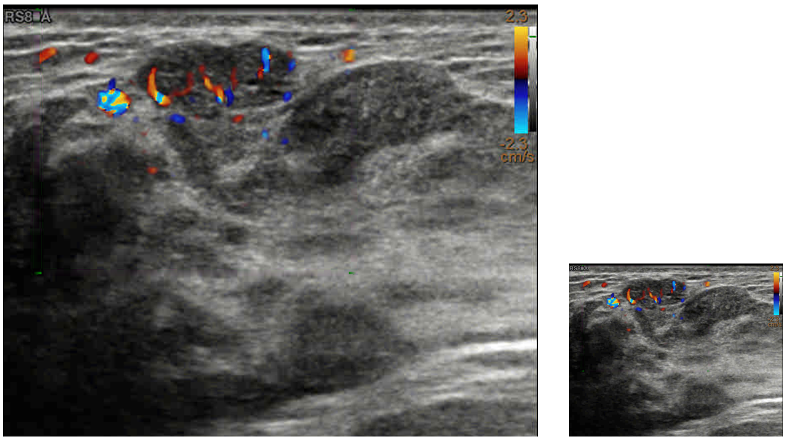

(a) (b)

Figure 4.9: (a) Original size of Power Doppler image 996×812. (b) 25% of actual size 249×203.

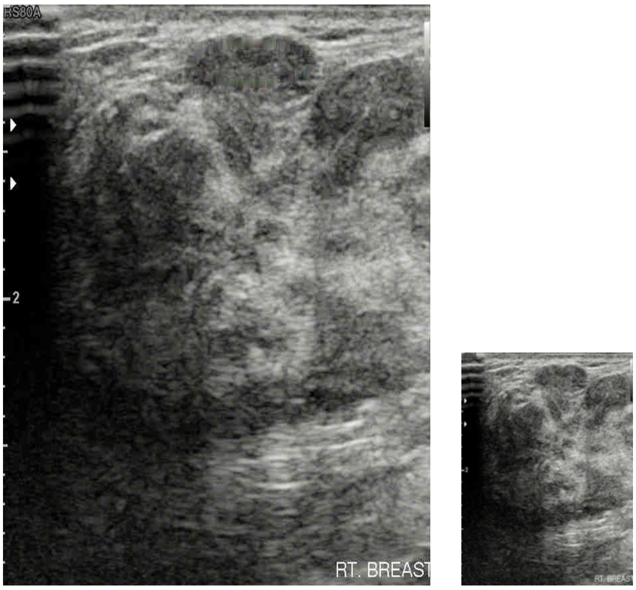

(a) (b)

Figure 4.10: (a) Original size of Elastography image 639×870. (b) 25% of actual size 160×218.

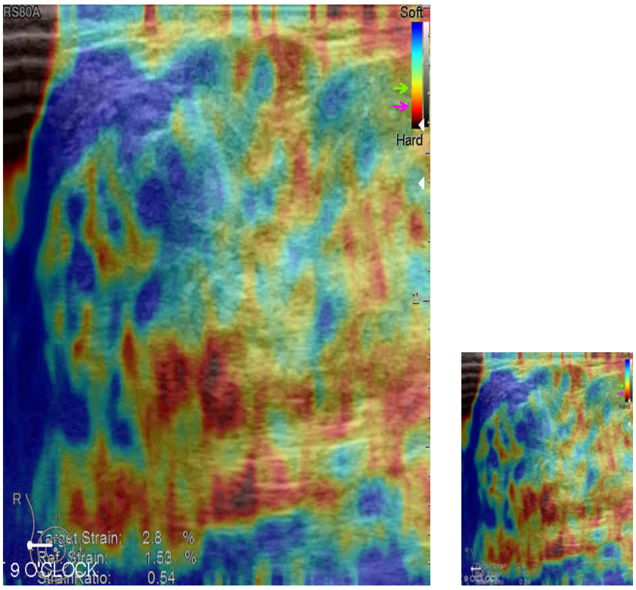

(a) (b)

Figure 4.11: (a) Original size of Elastography image 639×870. (b) 25% of actual size 160×218.

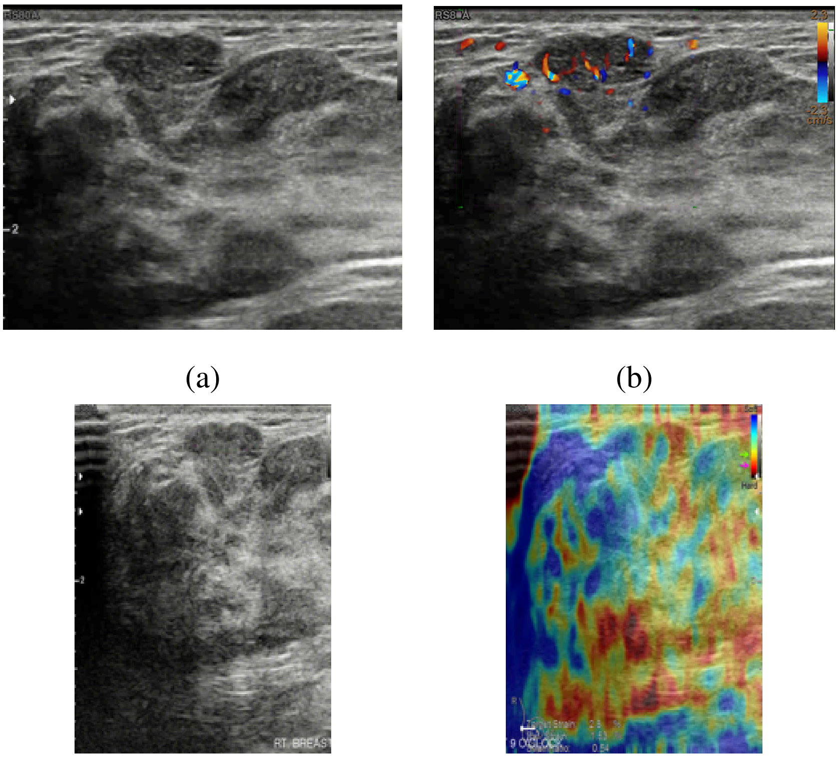

(a) (b)

(c) (d)

Figure 4.12: (a) convention US image. (b) Power Doppler image. (c) and (d) are conventional US and Elastography which are obtained simultaneously.

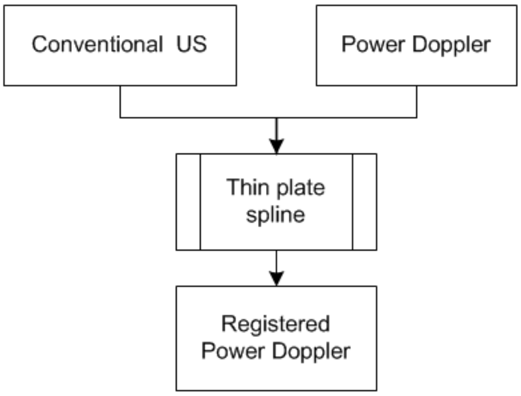

Figure 4.13: Image registration between conventional US and Power Doppler.

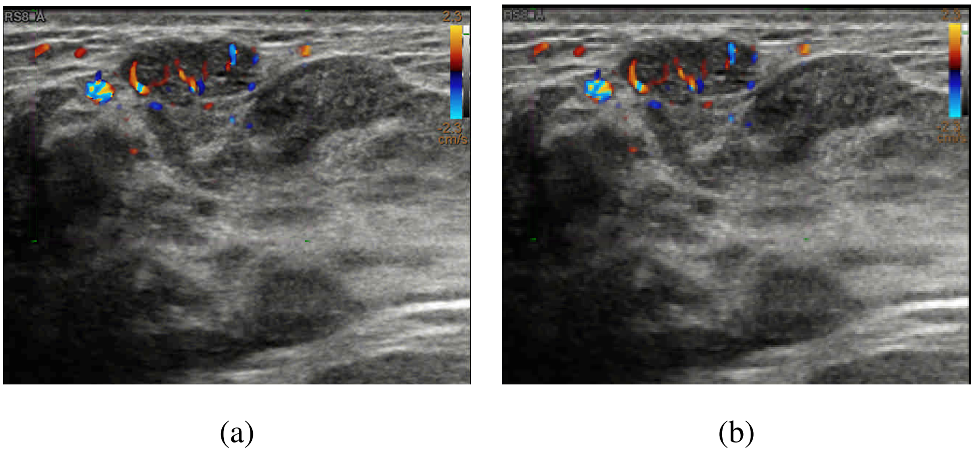
(a) (b)

Figure 4.14: (a) Original Elastography. (b) The result of image registration between conventional US and Power Doppler.

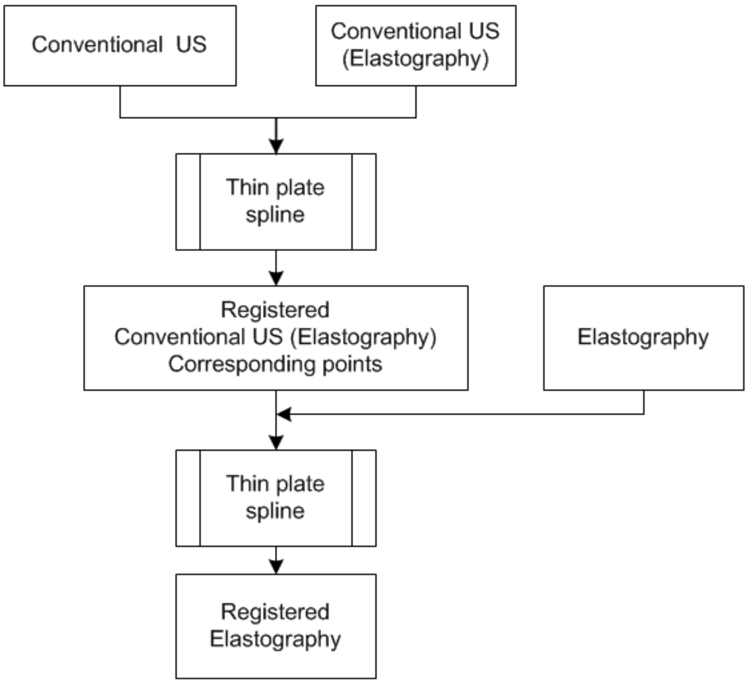

Figure 4.15: Image registration between conventional US and Elastography.

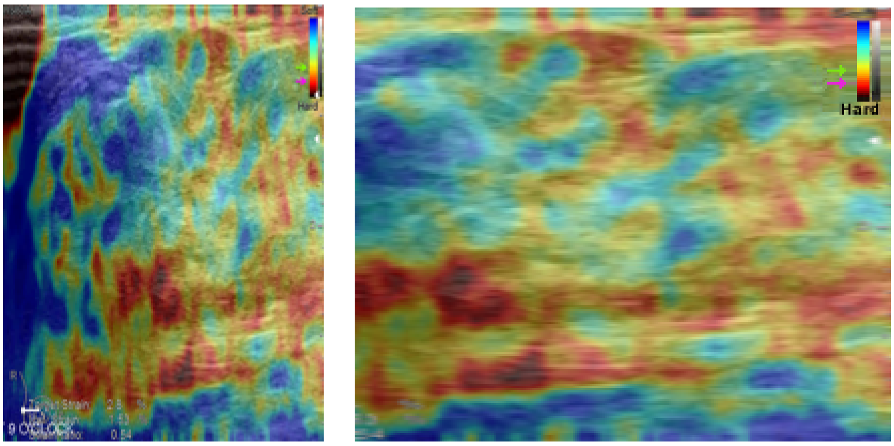

(a) (b)

Figure 4.16: (a) Original Elastography. (b) The result of image registration between conventional US and Elastography.

Chapter 5

Methodology

Active contours models are an efficient method for segmentation of ultrasound (US) images of breast cancer. However, the method produces inaccurate results if the seeds are initialized improperly (far from the true boundaries and close to the false boundaries). From [105] the method for integration of conventional US and Power Doppler for initialization for ACM performs good performance for correct initialization. However, its performance for the results of the breast cancer segmentation is average due to speckle noises. Therefore, the integration following breast cancer diagnosis is needed to improve the ability of ACM initialization and segmentation. In this research, we propose a novel initialization method based on the fusion of a conventional US image with Elastography and Power Doppler images.

5.1 Introduction

The goal of this paper is to set up the initial contour for active contour model in order to segment a malignant mass in a conventional US image. We invent the method by mocking up the breast cancer diagnosis using the significant information from the three US image modalities; conventional US, Elastography, Power Doppler images. At the beginning, these three images are processed for extracting useful information separately. Later on, the combining process is conducted to find the single common area as a representative of a breast cancer in conventional US image. Consequently, the utilization of the three US imaging modalities will be described separately until the the fusion process is invented. The overall process for US imaging modalities fusion is shown in Figure 5.1.

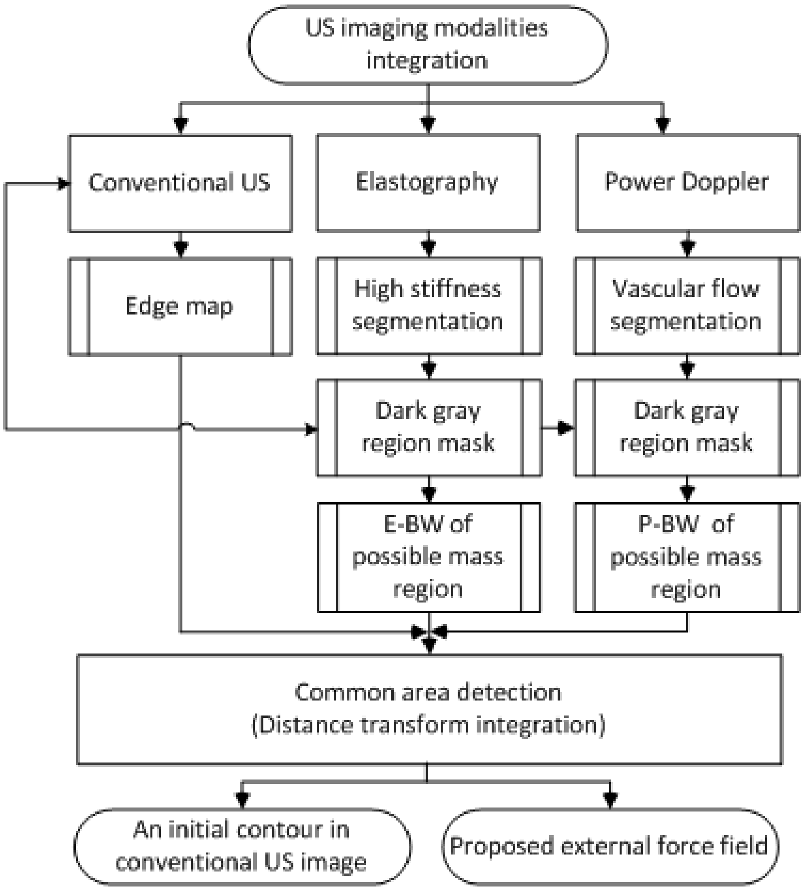

Figure 5.1: The process of developing an initial contour and proposed external force field of ACM for breast cancer detection utilizing the ultrasonic imaging modalities integration.

5.2 Binarized process

Since an integration process of these three images; conventional US, Ealastography and Power Doppler is performed by distance transform function, significant features from these image have to be attracted and transform to binary image.

5.2.1 Conventional US

Conventional US is used for two proposes; edge map for deriving external force for ACM; and dark gray mask for finding coarse common area between irregular mass in convention US image and Elastography image as well as in Power Doppler image.

Edge map of conventional US

The purpose of this paper is to segment malignant mass in conventional US image. Therefore, the binary edge of the image that is used as a gradient map for external energy of active contour model is required. Due to the sparkle noise and intensity inhomogeneities of the ROI, normal edge detection method may not be sufficient. Hence, we utilize a clustering based method for image segmentation, Fuzzy c-means (FCM) [106]. In addition, to compensate with the noise sensitive of FCM, the smoothing image, Gaussian blur method is applied. The optimal partition in image I can be obtained as follow,

$$I_{FCM} = \sum_{k=1}^{n} \sum_{i=1}^{c} (u_{i,k})^q d^2(x_k, v_i).$$

Where $X = \{x_1, x_2, ..., x_n\} \subseteq \Re^2$, n is the number of data items, c is the number of clusters with $2 \leq c \leq n$, $u_{i,k}$ is the degree of membership of x_k in the i_{th} cluster, q is a weighing exponent of each fuzzy membership, v_i is the prototype of the center of cluster i, $d^2(x_k, v_i)$ is a distance measure between object x_k and cluster center v_i. In order to set appropriate parameters of FCM which could be compatible to all datasets, the common parameters in 15-dataset are observed and then the parameters are tested again with other 30-dataset. The result of binary image of edge map extracting from I_{FCM} is showing in Figure 5.2 (a).

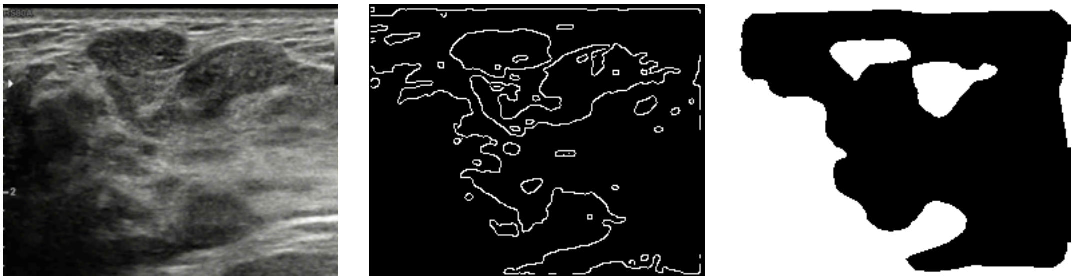

(a) (b) (c)

Figure 5.2: (a) Conventional US. (b) Edge map. (c) Dark gray mask.

Dark gray region mask

Under the assumption that the dark gray region would likely to be the mass region and the light gray should represent for normal tissue. First the conventional US is applied by Gaussian blur to smooth noise, and then utilized by the thresholding technique to create binary image with threshold value (t_M). The binary mask of dark gray scale region is shown in Figure 5.2 (b). Similar to edge map, the common t_M value is obtained from 30-dataset and follows testing by other 60-dataset.

5.2.2 Elastography

As a benign mass is softer than malignant mass but harder than normal tissue, the possible color in Figure 5.3 (a) and (b) that present high stiffness should be in the interval between light red and dark red.

Segmentation of high stiffness region

For color segmentation of Elastography image Figure 5.3 (a), first the image is converted from RGB color to HSV. Only Hue channel is used for the light red and dark red interval segmentation using thresholding technique. The common threshold value (t_H) is defined following the hue channel color bar in Figure 5.3(c). The binary image after thresholding is shown in Figure 5.4 (a).

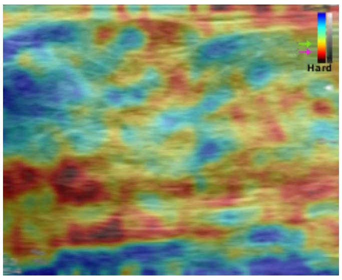

(a) Elastography.

(b) Color bar for stiffness of breast.

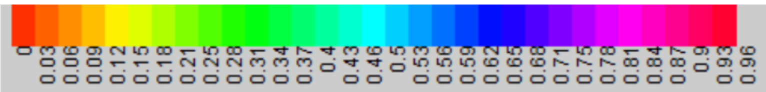

(c) Color bar for hue in HSV.

Figure 5.3: Elastography image segmentation.

Filter the common area of between conventional US and Elastography

Finally, the output binary image shown in Figure 5.4 (b) is obtained by applying dark gray mask in Figure 5.2 (c) to find roughly common area.

5.2.3 Power Doppler

The significant feature in Power Doppler is vascular flows that present as color areas in the gray-scale image 5.5 (a).

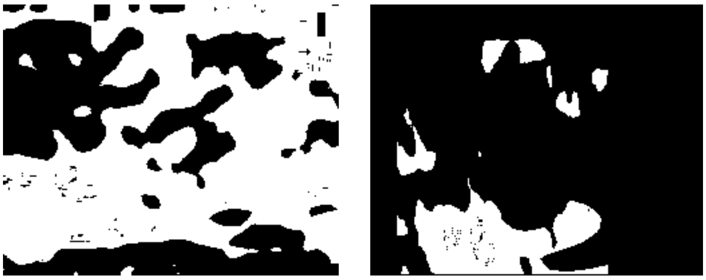

(a) (b)

Figure 5.4: Example of (a) high stiffness segmentation and (b) common area of high stiffness area and dark region area

(a) (b) (c)

Figure 5.5: (a) Power Doppler image. (b) Binarized Power Doppler image. (c) Common area of vascular flows area and dark region area.

Segmentation of vascular flows region

Basically, in gray-scale regions, the intensity values of R, G, and B channels are almost same. Contrast with the color objects which have different intensity values in the three channels with big variance. Therefore, the binary image (BW) extracting from the Power Doppler image (I) is done by finding non-identity value in the RGB-channel (IR, IG, IB) which has big variance. The output image is showing in Figure 5.5 (b).

```
1. Input $I$
2. for each pixel $i, j$, let $\sigma_{(i,j)} = \sqrt{Var\{IR_{(i,j)}, IG_{(i,j)}, IB_{(i,j)}\}}$
    (a) if $IR_{(i,j)} \neq IG_{(i,j)} \neq IB_{(i,j)}$ and $\sigma_{(i,j)} \geq t_\sigma$
        i. Let $BW_{(i,j)} = 1$
    (b) else
        i. Let $BW_{(i,j)} = 0$
```

Filter the common area of between conventional US and Power Doppler.

Similar to Elastography image, the output binary image shown in Figure 5.5 (c) is obtained by applying dark gray mask in Figure 5.2 (c) to find common area roughly.

Elimination of outliers in Power Doppler image

Based on reliable of region of Power dropper for automatic initialization. The outliers that locate in very far from a common region have to be eliminated shown in Figure 5.6. Detection

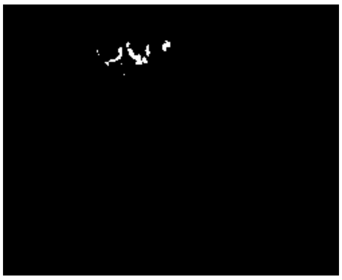

Figure 5.6: Binarized Power Doppler image after getting rid of outliers.

of outliers in D is performed by using Mahalanobis distance [107] as described following:

1. Input D-image.
2. Skeleton the vascular flows S_D by considering a number of points (n_D) in window size $n \times m$ with thresholding value t_v.
    (a) If $n_D < t_v$, Skeleton $\rightarrow p$ (1 pixel).
3. For each p in S_D (sorted by column of D).
    (a) Compute Mahalanobis distance for each point, $MD(p_i)$
    (b) Compute the 97.5%-Quantile Q of the Chi-square distribution.
        i. If $MD(p_i) > Q \& MD(p_i) > t_d$, outliers. Where t_d is a value used for verify that p_i is vary far from the common region.

5.3 Common area detection.

5.3.1 Soft intersection using distance transform algorithm

Following the over all assumption, a malignant mass should be located in the dark gray in conventional US, high stiffness mass which is the interval between light red and dark red in Elastography, as well as vascular flows regions present as color objects in Power Doppler. The most likely to be position for setting an initial contour would be obtained by applying soft intersection algorithm to the three binary images. In this paper, we utilize distance transform function [108] as a method to find common area among the thee Ultrasonography imaging modalities. Let $G = \{0, ..., n-1\} \times \{0, ..., m-1\}$ is a 2D grid, and $f : G \rightarrow R$ is an arbitrary

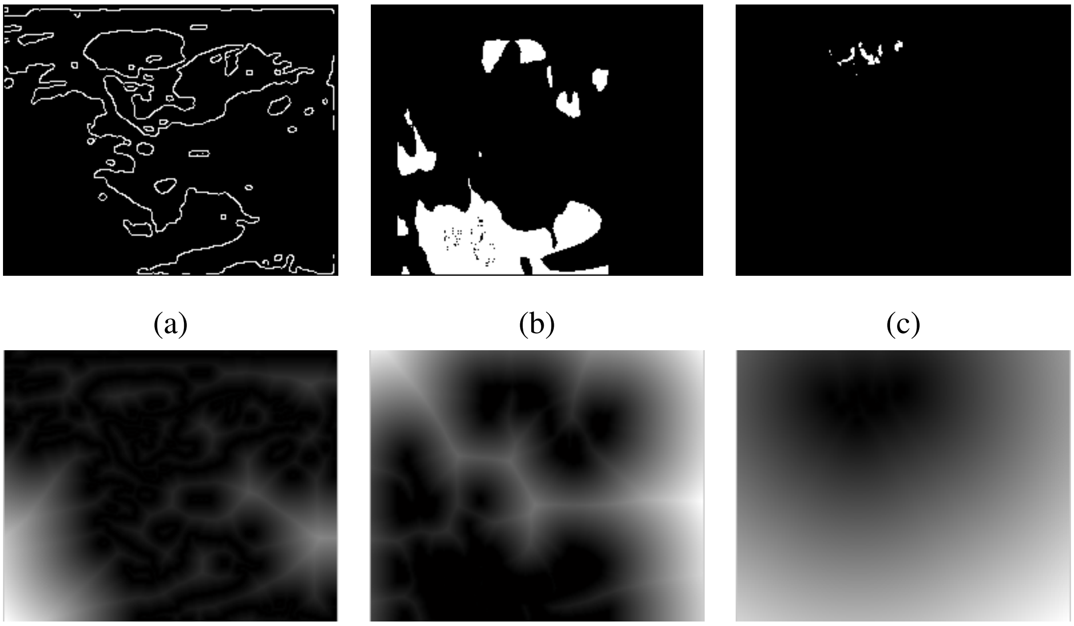
(a) (b) (c)

(d) (e) (f)

Figure 5.7: The results of Euclidean distance transform of (a) Edge Map, (b) Binarized Elastography, and (c) Binarized Power Doppler, are shown in (d)-(f) respectively.

function on the grid. The computation of the two dimensional Euclidean distance transform of f in a binary image is defined as,

$$D_f(x, y) = \min_{x',y'}((x - x')^2 + (y - y')^2 + f(x', y')).$$

In order to find soft intersection area, these three distant transform outputs are added together,

$$D_T(x_i, y_j) = W_E D_E(x_i, y_j) + W_{EG} D_{EG}(x_i, y_j) + W_{PD} D_{PD}(x_i, y_j).$$

The output of Euclidean distance transform of conventional US (D_E), Elastography (D_{EG}), Power Doppler (D_{PD}), are shown in Figure 5.7 (d)-(f) respectively.

The output of distance transform integration of D_E, D_{EG}, and D_{PD} with same value of weighting parameters ($W_E + W_{EG} + W_{PD} = 1$) is shown in Figure 5.8. Considering in gray-scale image, the common area of the three images represent in dark region.

An introductory example in Figure 5.9 demonstrates the advantages of the soft intersection for the binarized of conventional US, Elastography, and Power Doppler images in Figure 5.7 with the reference to the binary intersection. Clearly, the soft intersection in Figure 5.9

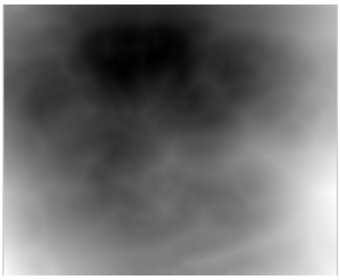

Figure 5.8: Output of distance transform integration with the same weighting of D_E, D_{EG}, and D_{PD}.

(f) produces an appropriate gray level image which can subsequently be used to initialize the active contour whereas the binary intersections in Figures 5.9 (d) and (e) are not suitable for initialization.

5.4 Estimation of an initial contour setting in conventional US

After distance transform integration, d_F is changed to gray scale image for detecting the most common past which is the dark region. The pipeline is started with small range of thresholding values that produce a binary image. After that each boundaries in binarized image are traced. Finally a boundary which is close to Power Doppler image is selected and then size of the selected boundary is resized.

To find the boundaries of the common area representing in dark region in Figure.5.8, first the thresholding method is used for generating binary image as shown in Figure 5.10 (a) with the range of threshold values (T). It is possible to find the suitable contour among the threshold values in T because the three distance transform outputs are transformed to gray scale image. After that, the boundaries of all dark regions in binary image could be traced shown in Figure 5.10 (b). The prospective boundary (B_o) could be extracted by considering; it should have high gradient along (B_o); big common area of B_o and the Power Doppler region (B_{CD}) shown in Fig. 5.10 (c); close center of B_o and B_{CD}; as well as, B_o is bigger than B_{CD}. The successful automatic thresholding is shown in Figure 5.10 (d), a representative boundary is B_o and its center is c_o. The main technique to find the common area of each trial initial contour with Power Doppler image is Partial Hausdorff distance and the overall method is described as,

5.4.1 Hausdorff distance

Hausdorff distance [109] measures the extent to which each point of a set points lines near some point of an image set and vice versa. Given two finite point set $A = \{a_1, ..., a_n\}$ and $B = \{b_1, ..., b_n\}$, the Hausdorff distance is defined as,

$$H(A, B) = max(h(A, B), h(B, A)),$$

where

$$h(A, B) = \max_{a \in A} \min_{b \in B} ||a - b||,$$

and $||.||$ is some underlying norm on the points of A and B. Throughout this research, we use the L_2 or Euclidean norm.

5.4.2 Modified Hausdorff distance

The modified Hausdorff distance is the best among possible distance measured based on the Hausdorff distance (MHD) [110]. It has high performance for object matching. The MHD is defined as,

$$f(h(A, B), h(B, A)) = max(h(A, B), h(B, A)),$$

and the distance between two sets is assigned as,

$$h(A, B) = \frac{1}{N_a} \sum_{a \in A} h(a, B).$$

5.4.3 Partial Hausdorff distance

In many problems, it is important to be able to identify instances of a model that are only partly visible (either due to occlusion or to failure of the sensing device to detect the entire object). Thus we wish to extend the definition of the Hausdorff distance to allow for the comparison of portions of two shapes called partial Hausdorff distance (PHD) [111]. This will allow both for scenes that contain multiple objects, and for objects that are partially hidden from view. For simplicity, we first consider just the forward distance $f_B(t) = h(t(B), A)$. Recall that, in effect each point of $t(B)$ is ranked by the distance to the nearest point of A, and the largest ranked point (the one farthest from any point of A) determines the distance.

A natural definition of the "partial distance" for K of the q points of $B(1 \leq K \leq q)$ is thus given by taking the $K-th$ ranked point of $t(B)$ (rather than the largest ranked one),

$$h_K(t(B), A) = \underset{b \in t(B)}{\overset{th}{\mathrm{K}}} \min_{a \in A} ||a - b||.$$

Where $K^{th}_{x \in x} f(x)$ denotes the $K-th$ ranked value of $f(x)$ over the set X. For example, the $n-th$ ranked value is the maximum, and the $n/2-th$ ranked value is the median (if X has n elements).

In order to compute the partial forward distance $h_K(t(B), A)$, we generally specify some fraction $0 < f_1 \leq 1$ of the points of B that are to be considered and set $K = [f_1 q]$. That is , wee seek the distance where some given fraction, f_1, of the model points $t(B)$ lie near image points. This fraction is set based on how much occlusion of the model we wish to tolerate (what fraction of the model can be missing from the image). Thus for example if $K = [0.9q]$, then $h_k(t(B), A) = \sigma$ when 90% of the points of $t(B)$ lie within distance σ of some point of A.

5.4.4 Automatic initialization for ACM.

5.4.5 Automatic initialization and segmenation

Consider a the fusion image d_F thresholded at some grey level T. Let us denote this binary image by $d_F(T)$, the corresponding edge map by $E_F(T)$ and a set of all continuous contours from $E_F(T)$ by $C_F(T)$. Our basic idea is that the best threshold is the one that minimizes the "distance" between $C_F(T)$ and the convex hull of the modified Doppler image.

The initial contour is generated as follows:

1. Input d_F-image, D-image, a sequence of thresholds $\mathbf{T}$.
2. Process the D-image Fig. 5.11 (b).
    (a) Calculate the convex hull in $D \rightarrow B_D$,
    (b) Calculate the centroid of $B_D \rightarrow c_{bd}$.
    (c) Calculate area of $B_D \rightarrow a_{bd}$.
3. For each T in $\mathbf{T}$
4. Threshold the fusion image and obtain $d_F(T)$.

   (a) Generate an edge map of $d_F(t) \rightarrow E_F$.

   (b) Find the all continuous contours belonging to $E_F \rightarrow C_F(T)$

   (c) From $C_F(T)$ find a contour B_o closest to the B_D Fig. 5.11 (c) - (e).

   (d) Evaluate the resulting contour using a decision tree.

   (e) Record B_o

5. If no contour selected, break.

6. Select the largest $B_o \rightarrow B_{init}$.

7. Resize $B_{init} = \gamma B_{init}$ (the contour is scaled by a factor γ with its centroid c_o being the origin) Fig. 5.11 (f).

B_o is evaluated using a decision tree based on the following features:

1. The average gradient of the gray level along B_o relative to the max gradient : $I(T)$.

2. The common area between B_o and B_D: A_{B_o,B_D}.

3. The distance between c_o and c_{bd} :$d_{c_o,c_{bd}}$.

4. The Boolean variable $L = B_D \in B_o$.

Classification And Regression Trees-CART

We train our decision tree (DT) by 30 additional US images using the Matlab function [112] designed to implement a conventional CART DT [113–116]. The following are the input parameters of the algorithm:

$$tree = (X, Y, 'AlgorithForCategorical', 'Pullleft', 'splitcriterion', 'gdi')$$

The corresponding decision tree and the thresholds (verified experimentally) are shown in Figure 5.12.

Note that in order to ensure that B_{init} is inside the tumor B_o is scaled by a factor γ. In principle, γ can be taken sufficiently small so that the snake evolves from the centroid. Our FM-balloon force will deliver the snake to the boundary even from a single point. However, in

Table 5.1: The evaluation of the size of an initial contour varying from 30-80%

Percentage of B_o	30	40	50	60	80
An initial contour is inside a mass (%)	100	100	95	80	67

order to improve the computation time, in practice, we considered $\gamma = 0.4$

An appropriate position to initiate contour should be inside a mass to avoid wrong extraction of snake caused by undesired edges nearby it. An initial contour, $init_B$ is a boundary that is resized from the representative contour (B_o) in Fig. 5.10 (d). The evaluation of assigning suitable size is conducted on 90-dataset in Table 5.1 shows 40% of B_o is the most appropriate.

Fig. 5.13 shows example of a sequence of contours (B_{t_c} crated by each thresholding value in blue dash line. The contour closest to the Doppler image (B_o) is depicted as a bold blue contour while an initial contour for snake that is resized B_o is shown in a bold green contour ($init_B$).

5.4.6 Balloon radial force

Recall that the traditional snake represented by Eq.(1) [84]. The proposed external force $E_{ext}(v(s))$ is composed of,

$$E_{ext}(v(s)) = E^1_{ext}(v(s)) + E^2_{ext}(x, y)).$$

where $E^1_{ext}(v(s))$ is the traditional gradient based force whereas $E^2_{ext}(x, y))$ is proportional to the distance between (x, y) and B_o so that $E^2_{ext}(x, y)) = 0$ if $(x, y) \in B_o$ and $E^2_{ext}(x, y)) = E^2_{max}$ if $(x, y) = c_0$, where E^2_{max} is evaluated experimentally(see Figure 5.14).

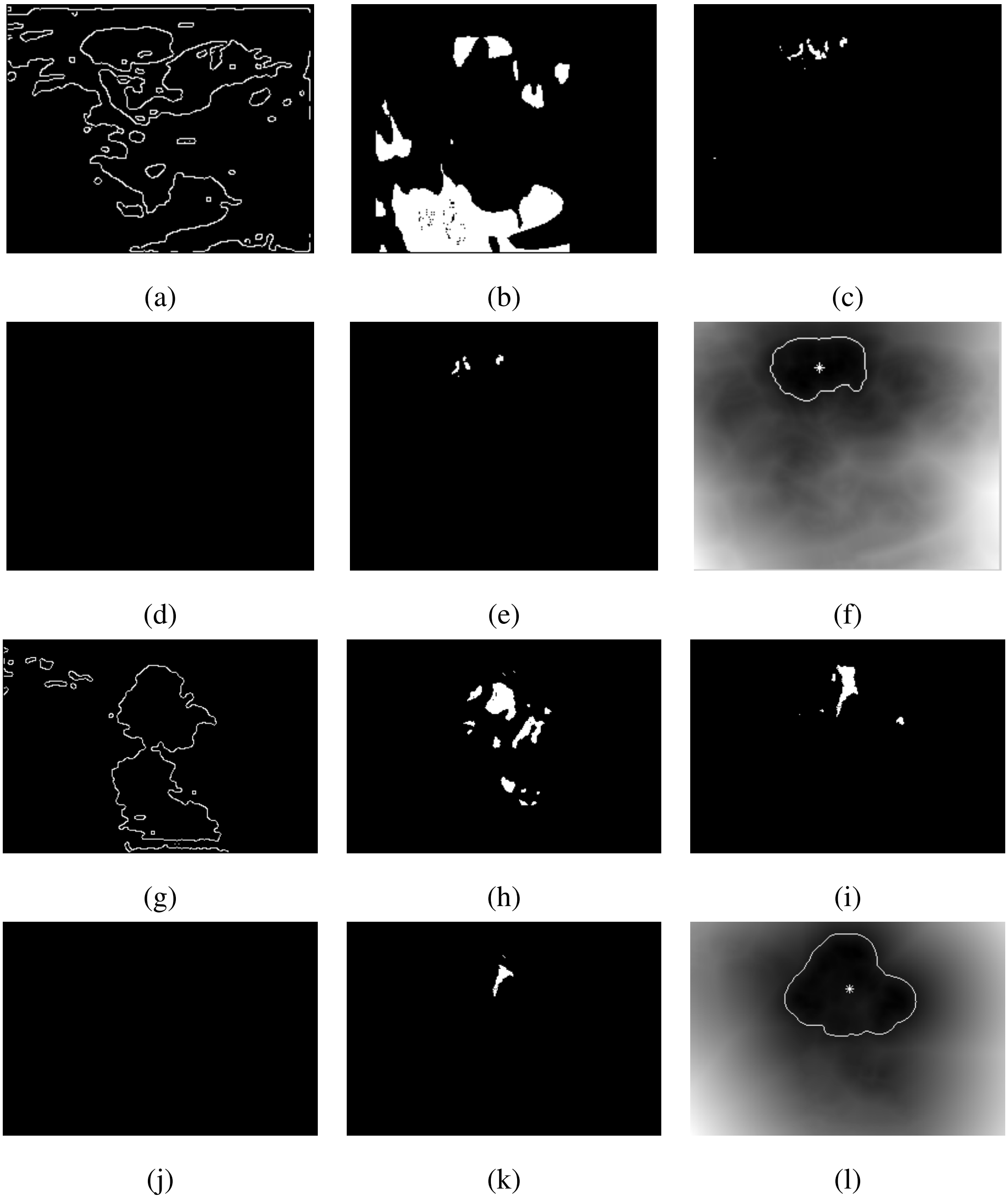

(a) (b) (c)

(d) (e) (f)

(g) (h) (i)

(j) (k) (l)

Figure 5.9: Soft and hard(binary)intersection(a) U, (b) E, (c) D, (d) hard intersection of U, E, and D, (e) hard intersection of E, and D, and (f) soft intersection of U, E, and D.

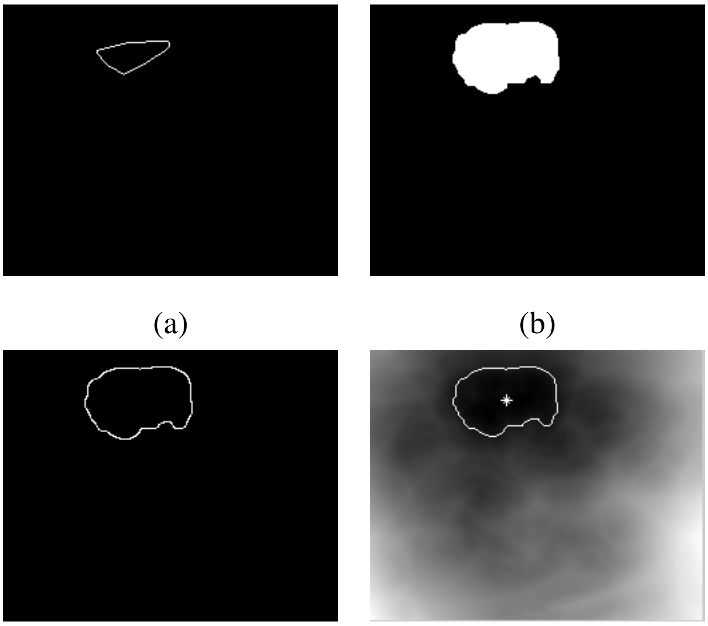

(a) (b)

(c) (d)

Figure 5.10: a) E_D. (b)Binarized image. (c)E_F. (d) B_o

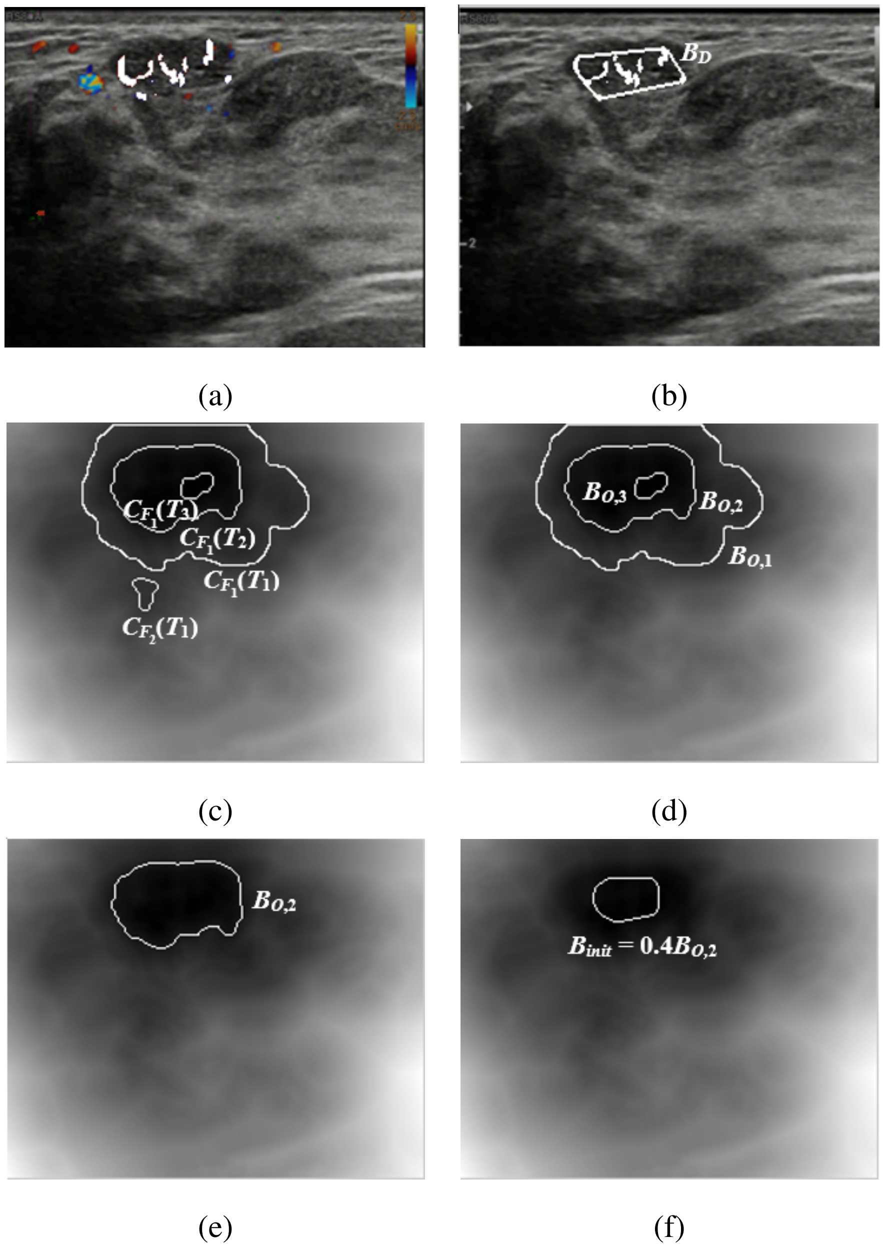

Figure 5.11: (a) D-image without the outliers (b) the convex hull B_D (c) contours $C_{F_1}(T_1), C_{F_2}(T_1)$-obtained for $T = T_1$,$C_{F_1}(T_2)$ and $C_{F_1}(T_3)$ obtained for $T = T_2$ and $T = T_3$ (d) B_{o_1},B_{o_2} and B_{o_3} are the closest to B_D (e) $B_{o,2}$ passes the decision tree (f) $B_{init} = \gamma B_{o,2}$

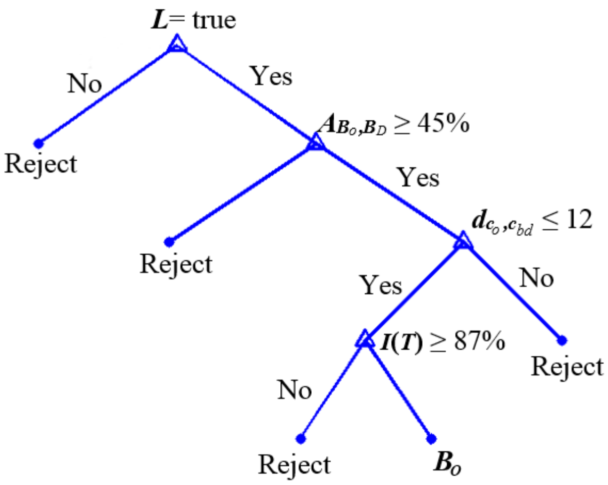

Figure 5.12: Decision tree is created by the CART algorithm [113]

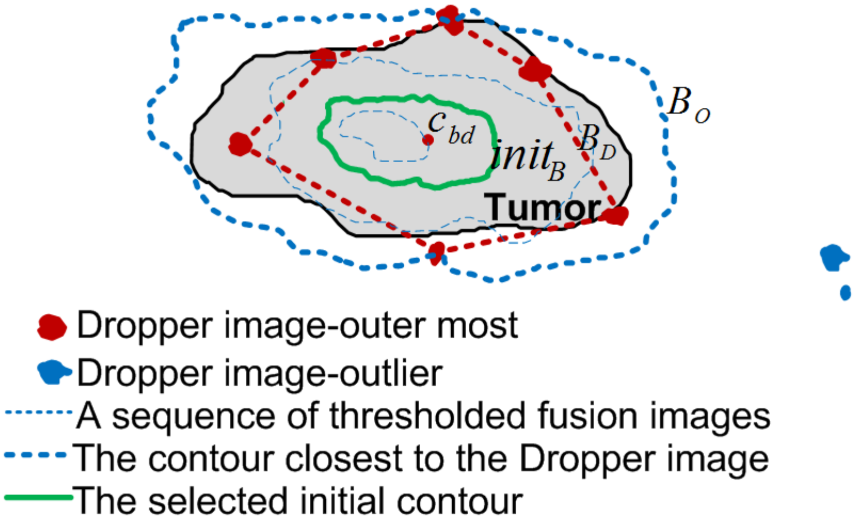

Figure 5.13: Example of contour selection in automatic initialization.

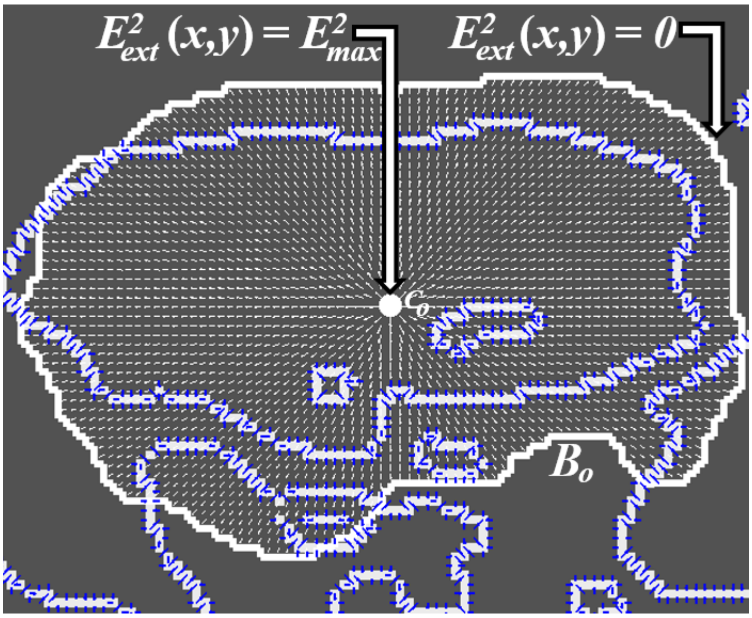

Figure 5.14: External energy $g(x, y)$, proposed external force is created from center of outer boundary to outer boundary, E^1_{ext} is shown in blue, and E^2_{ext} is depicted in white.

Chapter 6

Performance measures

In order to compare the fusion method (FM) with the conventional algorithms we introduce the following performance measures.

6.1 Contour based accuracy measures

The Hausdorff distance given by

$$dist_{H_1}(X,Y) = \max\{\max_{a\in X}\min_{b\in Y} \| a{-}b \|, \max_{b\in Y}\min_{a\in X} \| a{-}b \|\} \tag{6.1}$$

where $\| \ \|$ denotes the Euclidean distance, X the ground truth contour, and Y the snake contour. The averaged Hausdorff distance is defined by

$$dist_{H_2}(X,Y) = \max\{\frac{\sum\limits_{a\in X}\min\limits_{b\in Y} \| a{-}b \|}{L_X}, \frac{\sum\limits_{b\in Y}\min\limits_{a\in X} \| a{-}b \|}{L_Y}\}, \tag{6.2}$$

where L_X, L_Y is the length of the true contour, and the resulting contour, respectively. The relative Hausdorff distance is given by

$$dist_{H_3}(X,Y) = \frac{dist_{H_1}(X,Y)}{L_X}\xi, \tag{6.3}$$

where $\xi = 1000$ is the normalizing coefficient. The distance evaluates the relative importance of the difference between the two curves. For instance, if $dist_{H_1}(X,Y) = 10$, and $L_X = 100$ pixels, the error is unacceptable, however, if for instance, $L_X = 10000$, then $dist_{H_3}(X,Y)$ is appropriate. The importance of the Hausdorff distance in comparing planar curves is parametrization invariance. Although $dist_{H_1}$ is not a distance in a rigorous mathematical sense (it does not satisfy the triangle inequality), [117] shows that it is the best for matching curved objects. The contour-based true positive rate is:

$$TP_c = \frac{TP_Y}{N_Y}, \tag{6.4}$$

where TP_Y is the number of true positive pixels, and N_Y is the total number of pixels belonging to the resulting active contour (in practice we consider $L_X = N_X$ and $L_Y = N_Y$).

6.2 Region based accuracy measures

The most used metric in validating medical segmentations [118] is the Dice coefficient given by

$$DICE = \frac{2TP}{2TP + FP + FN}, \tag{6.5}$$

where TP, FP, and FN are the region-based true positive, false positive, and false negative. We also use the Jaccard index given by

$$JAC = \frac{TP}{TP + FP + FN}, \tag{6.6}$$

and the sensitivity given by

$$SEN = \frac{TP}{TP + FN}. \tag{6.7}$$

Finally, we employ a region based averaged Hausdorff distance, given by

$$dist_{H_R}(R_X, R_Y) = \max\{\frac{\sum\limits_{a \in R_X} \min\limits_{b \in R_Y} \parallel a - b \parallel}{A_{R_X}}, \frac{\sum\limits_{b \in R_Y} \min\limits_{a \in R_X} \parallel a - b \parallel}{A_{R_Y}}\}, \tag{6.8}$$

where R_X and R_Y are the regions corresponding to the contours X and Y, respectively. A_{R_X} and A_{R_Y} are the areas of R_X and R_Y, respectively.

6.3 Performance of the initialization procedure

The performance of the initialization is evaluated for the entire series of images by N_{corr}, defined as the percentage of images for which the internal and external seeds were correctly differentiated, S_{corr}, the percentage of images for which the contour was correctly segmented (the final snake is considered correct if $dist_{H_2}(X, Y) \leq 3$), and the computational time T_{comp}.

As noted above, the segmentation accuracy depends not only on initialization, but on the segmentation model as well. For instance, the level set method, clustering, watershed segmentation, region growing, and edgeless active contours may benefit from the proposed FM. However, this is out of the scope of this paper. At present, the model is focused on the parametric active contours.

Chapter 7

Results and Discussion

The algorithm has been tested on 90 US images of breast cancer from 90 different patients obtained by a Philips iU22 ultrasound machine at the Thammasat University Hospital. The resolution ranges from 200×200 to 300×400 pixels.The ground truth contours have been hand-drawn by leading radiologists with the Department of Radiology of Thammasat University.

7.1 Evaluation and discussion

The proposed method (FM) has been tested against four state-of-the-art initialization models, namely, center of divergence (CoD) [11], force field segmentation (FFS) [10], Poisson inverse gradient (PIG) [12], and quasi automatic initialization (QAI) [13, 14], using the performance measures in chapter 6. In order to prove the efficiency of the fusion radial force (FRF), we compare with the Vector Field Convolution (VFC) snake [8] and the recent Adaptive Diffusion Flow (ADF) [9] methods, which have been proven to be superior to GVF [5], Normal Gradient Vector Flow [94], Infinity Laplacian GVF [95], and Harmonic Gradient Vector Flow [96]. Figure 7.1 is an example, comparing the initialization and the resulting snake produced by the FM/FRF with CoD/VFC, FFS/VFC,PIG/VFC, and QAI/VFC. Figures 7.1 (a) (b) show a US image with a "false" tumor on the right side of the image and a shadow at the lower left corner, characterized by grayscale comparable with a gray level of the true tumor. The resulting edge map in Figure 7.1 (c) shows multiple irregular contours. Clearly, if a contracting snake is initialized at the boundary of the image, it will attach itself to a wrong object and produce a totally inappropriate contour. Therefore, this US image requires a high quality initial snake, preferably expanding from the inside of the true contour. The CoD and FFS produce multiple seeds at the CoDs (Figure 7.1 (e), (f)). However, due to noise, the corresponding multiple snakes are unable to merge (Figure 7.1 (j), (k)). In turn, the PIG misses the true tumor and generates the initial contour inside a false object (Figure 7.1 (g)). Therefore, the resulting snake is inappropriate (Figure 7.1 (l)). Finally, QAI requires one user-defined point inside the actual object. Due to this, QAI generates the initial contour around a correct location of the tumor. Since QAI is based on a "skeleton" of the object, which connects the CoDs, the method wrongly includes a CoD located outside the object Figure 7.1 (h). Consequently, the expanding snake grows outside the tumor and partially attaches to a false boundary (Figure 7.1 (m)). The FM initialization method outperforms the above techniques because it has more information about the location of the tumor. Although the low intensity mask in Figure 5.2 (b) can not localize the tumor, the combination of the Doppler and elasticity images excludes the artifact (false tumor), unwanted shadows and produces an appropriate initial contour B_{init}. Finally, the proposed DT verifies the candidate contour using supplementary features.

Tables 1-3 in the forthcoming sections illustrate numerical tests of the proposed method vs. the above mentioned techniques, using the initialization and accuracy measures (8)-(15) in Section 5. For every measure, we calculate the mean μ and the standard deviation σ. For all evaluation measures related to FM $\sigma/\mu < 1$, which indicates a low spread of the results.

Table 7.1 demonstrates the advantages of the proposed initialization method. The CoD and FFS failed, whereas QAI and PIG yield a lower performance in both N_{corr} and S_{corr}. All tested methods have been implemented on the MathLab platform, using a CPU AMD PRO A8-8600B R6, 1.6 GHz with 8GB RAM and 64-bit OS. The FM is the second best by speed, but significantly better in all other categories, including correctly initialized and correctly segmented images. Tables 7.2 and 7.3 show the performance of FM/FRF, CoD/VFC, FFS/VFC, PIG/VFC and QAI/VFC. Clearly, the results produced by the reference methods are poor and are not even close to the proposed algorithm. For instance, in terms of $dist_{H_2}$, the average accuracy of the FM is 2.4 pixels, whereas CoD, FFS, PIG, and QAI produce 321.6, 486.57 (totally wrong!), 58.5, and 82.23, respectively.

7.1.1 Impact of the radial force

The next important question is the impact of the FRF. Figure 7.2 compares segmentation produced by the proposed FRF with that produced by VFC and ADF. Note the initial contour is

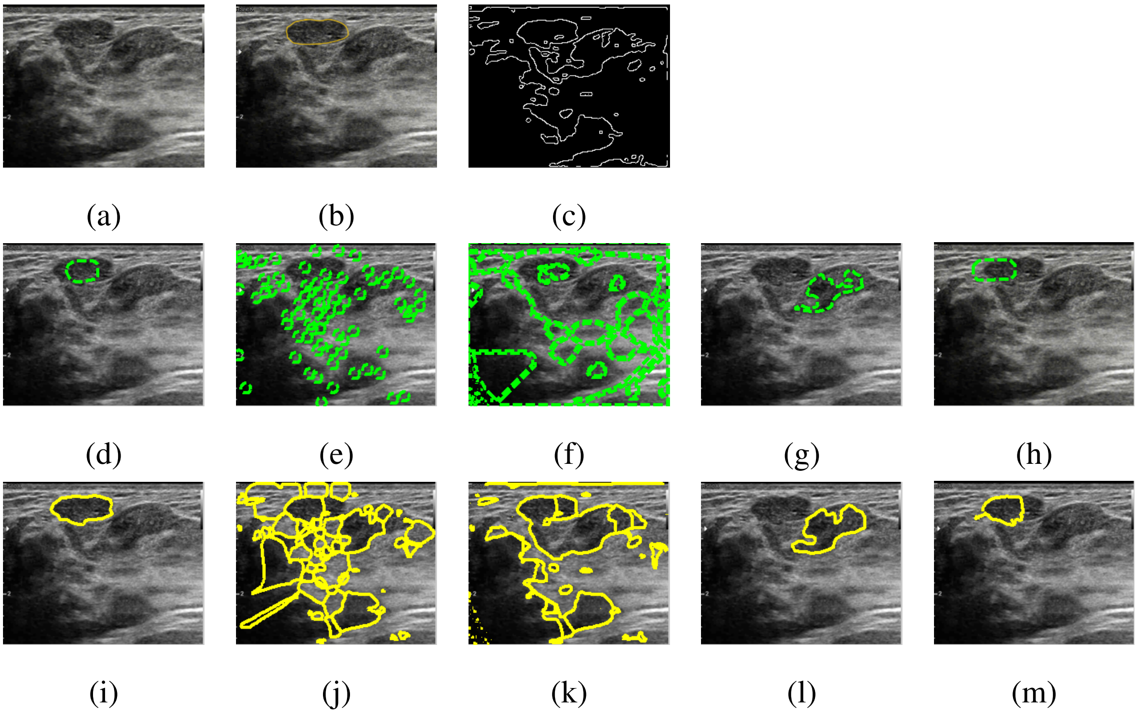

Figure 7.1: (a) US image, (b) ground truth, (c) U_{edge}, (d) FM-initialization, (e) CoD initialization,(f) FFS-initialization, (g) PIG-initialization (h) QAI-initialization. Segmentation results: (i) FM/FRF (j), CoD/VFC, (k) FFS/VFC,(l)-PIG/VFC, (m) QAI/VFC

Table 7.1: Efficiency of initialization. FM vs. reference methods

Model	Initialization measures				
	Comp. time T_{com}, sec			Correctly initialized N_{corr},%	Correctly segmented S_{corr},%
	μ	σ	σ/μ		
FM	11.39	2.07	0.18	92.22	84.44
CoD	17.72	14.07	0.79	0.00	0.00
FFS	19.53	9.65	0.49	0.00	0.00
PIG	9.17	1.58	0.17	26.67	16.67
QAI	145.23	14.89	0.10	42.22	22.44

obtained by FM. Tables 7.4, 7.5, and 7.6 clearly demonstrate that the FM-based initialization improves ADF and VFC. For instance, FM/VFC segments 56% of the images, whereas the best initialization using QAI/VFC detects only about 22%. However, the performance is still

Table 7.2: FM vs. reference methods. Contour based measures

Model	Contour based measures											
	H_1			H_2			H_3			TP_C		
	μ	σ	σ/μ	μ	σ	σ/μ	μ	σ	σ/μ	μ	σ	σ/μ
FM	7.54	3.40	0.45	2.40	0.95	0.39	8.27	3.43	0.41	80.73	9.32	0.11
COD	176.31	27.98	0.16	321.60	121.00	0.38	299.16	108.72	0.36	9.30	6.30	0.68
FFS	171.80	31.51	0.18	294.17	182.47	0.62	239.57	81.24	0.34	6.69	4.70	0.70
PIG	77.48	39.01	0.50	58.50	39.52	0.67	127.76	89.84	0.70	16.58	12.54	0.76
QAI	71.40	31.18	0.44	82.23	132.10	1.61	142.99	187.69	1.31	25.66	34.56	1.35

Table 7.3: FM vs. reference methods. Region based measures

Model	Region based measures											
	$Jaccard$			$Dice$			SEN			H_R		
	μ	σ	σ/μ	μ	σ	σ/μ	μ	σ	σ/μ	μ	σ	σ/μ
FM	0.89	0.07	0.78	0.90	0.08	0.88	89.99	4.20	0.05	0.24	0.14	0.58
COD	0.17	0.09	0.59	0.28	0.14	0.50	31.76	21.58	0.68	74.16	28.94	0.39
FFS	0.16	0.12	0.75	0.27	0.17	0.63	36.68	29.03	0.79	62.57	34.51	0.55
PIG	0.1	0.24	2.40	0.15	0.29	1.93	12.28	24.72	2.01	42.35	11.50	0.27
QAI	0.34	0.36	1.06	0.38	0.41	1.08	38.27	34.56	0.90	44.41	38.32	0.86

substantially lower than the 84% produced by FM/FRF. The accuracy of VFC has been also improved (see an impressive decrease of H_2 from 39 pixels (PIG/VFC) to 9.58 (FM/VFC) in Table 7.5). However, the proposed FM/FRF is still the winner with $H_2 = 2.4$ and with the smallest standard deviation of about 0.95. As a matter of fact, for the contour based measures, FM has the smallest ratio σ/μ in all categories.

7.1.2 Relative impact of different modalities

An important question is whether the FM/FRF requires all three image modalities, and which modality is the most important. Tables 7.7, 7.8, and 7.9 show the accuracy of the proposed method applied to combinations (U,E), (U,D), etc. Clearly, combining the three types of images produces the best accuracy. Interestingly enough, (E,D) is the second best in the accuracy. However, the segmentation procedure uses a mask produced by the US image. Since this com-

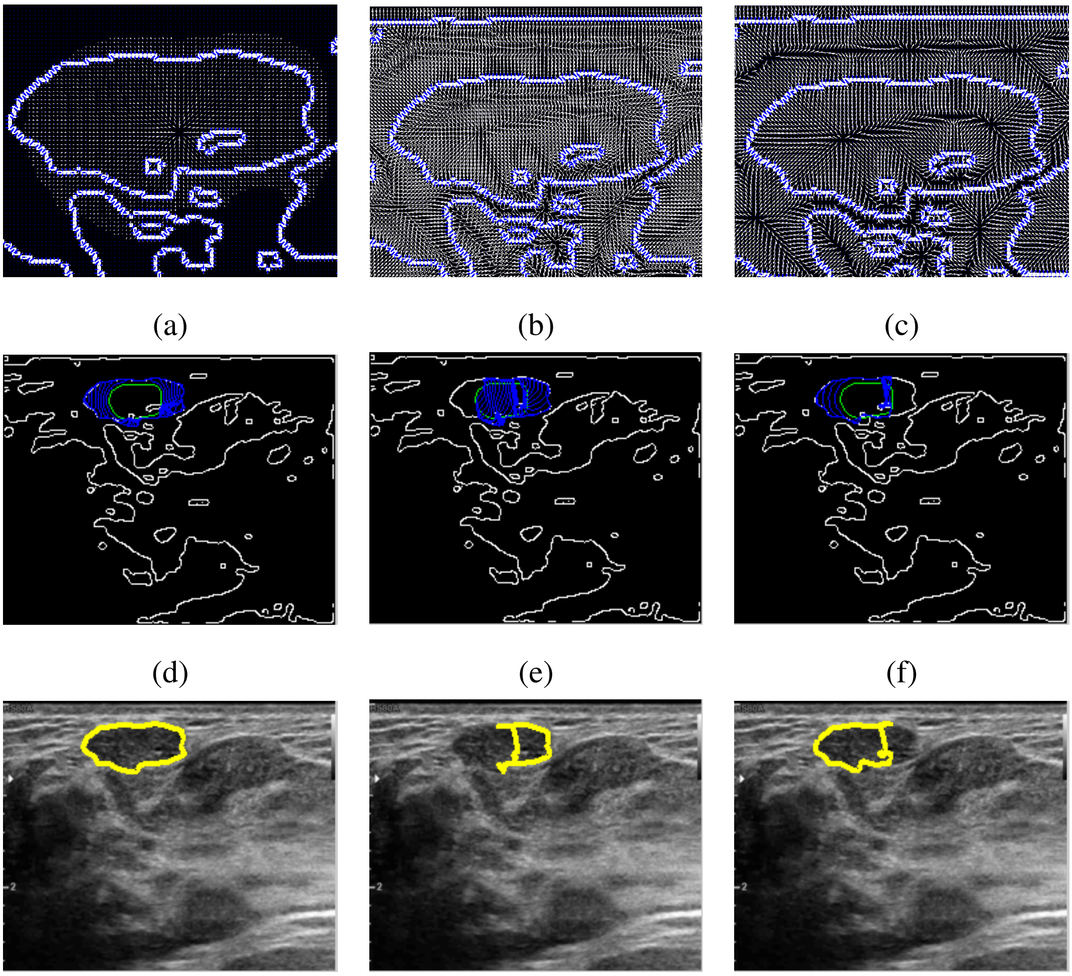

(a) (b) (c)

(d) (e) (f)

(g) (h) (i)

Figure 7.2: Force field: (a)FRF, (b) VFC, (c) ADF; snake evolution: (d)FRF, (e) VFC, (f) ADF; segmentation results: (g) FRF, (h) VFC, (i) ADF.

Table 7.4: Impact of the radial force

Model	Segmentation measures			
	Comp. Time T_{com}, sec			Correctly segmented S_{corr},%
	μ	σ	σ/μ	
FM	0.09	0.03	0.33	84.44
VFC	0.08	0.03	0.37	56.62
ADF	0.11	0.08	0.73	43.30

Table 7.5: Impact of the radial force. Contour based measures

Model	Contour based measures											
	H_1			H_2			H_3			TP_C		
	μ	σ	σ/μ	μ	σ	σ/μ	μ	σ	σ/μ	μ	σ	σ/μ
FM	7.54	3.40	0.45	2.40	0.95	0.39	8.27	3.43	0.41	80.73	9.32	0.11
VFC	20.09	18.53	0.92	6.98	9.58	1.37	13.61	10.89	0.80	62.05	28.51	0.46
ADF	24.69	20.06	0.81	7.20	9.65	1.34	14.16	10.40	0.73	61.26	25.61	0.42

Table 7.6: Impact of the radial force. Region based measures

Model	Region based measures											
	$Jaccard$			$Dice$			SEN			H_R		
	μ	σ	σ/μ	μ	σ	σ/μ	μ	σ	σ/μ	μ	σ	σ/μ
FM	0.89	0.07	0.78	0.90	0.08	0.88	89.99	4.20	0.05	0.24	0.14	0.58
VFC	55.87	28.92	0.52	66.02	29.17	0.44	65.71	23.71	0.36	4.80	4.97	1.03
ADF	53.54	22.75	0.42	66.82	22.51	0.34	62.92	20.09	0.32	5.04	4.46	0.88

bination implicitly uses the U-image, it is incorrect to say that the algorithm is based solely on (E,D). This complies with recent clinical research [65], [66] which reports that the Doppler image alone does not significantly contribute to categorization of solid masses.

Table 7.7: Efficiency of initialization for different combinations of the modalities

Model	Initialization measures				
	Comp. Time T_{com}, sec			Correctly initialized N_{corr},%	Correctly segmented S_{corr},%
	μ	σ	σ/μ		
FM(U,E,D)	11.39	2.07	0.18	92.00	84.44
FM(E,D)	11.29	1.78	0.16	80.00	73.33
FM(U,E)	11.26	1.91	0.17	13.33	11.11
FM(U,D)	11.30	1.79	0.16	53.33	48.88

Table 7.8: Contour based accuracy for different combinations of the modalities

Model	Contour based measures											
	H_1			H_2			H_3			TP_C		
	μ	σ	σ/μ	μ	σ	σ/μ	μ	σ	σ/μ	μ	σ	σ/μ
FM(U,E,D)	7.54	3.40	0.45	2.40	0.95	0.39	8.27	3.43	0.41	80.73	9.32	0.11
FM(E,D)	12.72	9.49	0.75	3.78	3.27	0.86	13.89	12.74	0.92	77.62	22.01	0.28
FM(U,E)	42.95	41.50	0.97	30.61	40.93	1.34	138.81	102.03	0.73	9.60	26.54	2.76
FM(U,D)	17.89	10.00	0.56	5.58	3.69	0.66	19.99	14.78	0.74	56.56	31.65	0.56

Table 7.9: Region based accuracy for different combinations of the modalities

Model	Region based measures											
	$Jaccard$			$Dice$			SEN			H_R		
	μ	σ	σ/μ	μ	σ	σ/μ	μ	σ	σ/μ	μ	σ	σ/μ
FM(U,E,D)	0.89	0.07	0.78	0.90	0.08	0.88	89.99	4.20	0.05	0.24	0.14	0.58
FM(E,D)	0.81	0.08	0.10	0.88	0.08	0.09	89.60	4.20	0.05	4.01	7.70	1.92
FM(U,E)	0.36	0.29	0.80	0.47	0.31	0.66	77.42	41.15	0.53	37.10	21.53	0.58
FM(U,D)	0.60	0.21	0.35	0.73	0.21	0.29	84.21	14.79	0.17	7.40	7.67	1.04

7.1.3 Limitations of the method

The method requires a good quality Doppler image D_{raw}. If D_{raw} does not present a well-defined cluster of Doppler spots, the procedure works in the $U-E$ mode, which may reduce the accuracy of segmentation (see Table 7.7). Besides, some low grade cancers may not appear in the Doppler images. For instance, [119] reports that “four percent of the cancers had no detectable”.

Chapter 8

Conclusion and Futer Work

8.1 Conclusion

The initialization algorithms for the Ultrasound images often rely on gray levels and textures, to place the seed points inside the tumor. Saliency and feature maps also have been proposed. Besides these techniques, a special vector field to hybridize the GVF and the texture. A few papers related to a specific medical image processing task use the typical position of a human organ in the US images. However, these models are image dependent and may not work if strong noise is present. Therefore, this paper proposes a new fast algorithm for automatic initialization, which combines the conventional grayscale US image with the corresponding elasticity and Doppler images. The technique makes it possible to locate the initial contour inside the tumor, close enough to the true boundaries to ensure convergence of the active contour. The paper also introduces a modification of the balloon type active contour, based on a combination of the radial force derived from the fusion image and the GVF-type force.

We propose new automatic procedure for initialization of active contours applied to segmentation of ultrasound images of breast cancer, outperforms preceding algorithms. The procedure includes FM initialization and a radial force based on the fusion of the conventional US, Doppler, and elasticity images. In terms of accuracy, the FM is better than CoD, FFS, PIG, and QAI. Although it requires training the decision tree, the training is also automatic and does not involve any human intervention, except providing data. We conjecture that the proposed algorithm is applicable to similar US images without any modifications.

8.2 Future work

Although the proposed method works well in term of accuracy for initialization and segmentation, the runtime compared to PIG is one of FM drawbacks. Therefore, we would like to investigate more to reduce runtime of FM to be as small as possible. Moreover, the collection of a number of datasets including conventional US, Elastography, and Power Doppler is very important for information analysis in order to gain more knowledge of the breast cancer diagnosis leading to better modeling for improving accuracy of FM.

Bibliography

[1] *Breast cancer facts and figures*, `https://www.cancer.org/research/cancer-facts-statistics/breast-cancer-facts-figures.html`, Oct. 2017.

[2] J. R. Eisenbrey, J. K. Dave, and F. Forsberg, "Recent technological advancements in breast ultrasound," *Ultrasonics*, vol. 70, pp. 183 –190, 2016.

[3] Z. L. Wang, L. Sun, Y. Li, and N. Li, "Relationship between elasticity and collagen fiber content in breast disease: A preliminary report," *Ultrasonics*, vol. 57, pp. 44 –49, 2015.

[4] N. Cho, M. Jang, C. Y. Lyou, J. S. Park, H. Y. Choi, and W. K. Moon, "Distinguishing benign from malignant masses at breast us: Combined us elastography and color doppler usłnfluence on radiologist accuracy," *Radiology*, vol. 262, no. 1, pp. 80 –90, 2012.

[5] C. Xu and J. L. Prince, "Snakes, shapes, and gradient vector flow," *IEEE TRANSACTIONS ON IMAGE PROCESSING*, vol. 7, no. 3, pp. 359–369, 1998.

[6] ——, "Generalized gradient vector flow external forces for active contours," *Signal Processing*, vol. 71, no. 2, pp. 131 –139, 1998.

[7] J. Tang, "A multi-direction {gvf} snake for the segmentation of skin cancer images," *Pattern Recognition*, vol. 42, no. 6, pp. 1172 –1179, 2009, Digital Image Processing and Pattern Recognition Techniques for the Detection of Cancer.

[8] B. Li and S. T. Acton, "Active contour external force using vector field convolution for image segmentation," *IEEE Transactions on Image Processing*, vol. 16, no. 8, pp. 2096–2106, 2007.

[9] Y. Wu, Y. Wang, and Y. Jia, "Adaptive diffusion flow active contours for image segmentation," *Computer Vision and Image Understanding*, vol. 117, no. 10, pp. 1421–1435, 2013.

[10] C. Li, J. Liu, and M. D. Fox, “Segmentation of external force field for automatic initialization and splitting of snakes,” *Pattern Recognition*, vol. 38, no. 11, pp. 1947 –1960, 2005.

[11] G. Xingfei and T. Jie, *An automatic active contour model for multiple objects*, 2002.

[12] B. Li and S. T. Acton, “Automatic active model initialization via poisson inverse gradient,” *IEEE Transactions on Image Processing*, vol. 17, no. 8, pp. 1406–1420, 2008.

[13] C. Tauber, H. Batatia, and A. Ayache, *A general quasi-automatic initialization for snakes: Application to ultrasound images*, 2005.

[14] ——, “Quasi-automatic initialization for parametric active contours,” *Pattern Recognition Letters*, vol. 31, no. 1, pp. 83 –90, 2010.

[15] J. Noble and D. Boukerroui, “Ultrasound image segmentation: A survey,” *IEEE Transactions on Medical Imaging*, vol. 25, pp. 987 –1010, 2006.

[16] J. Shan, H. Cheng, and Y. Wang, “Completely automated segmentation approach for breast ultrasound images using multiple-domain features,” *Ultrasound in Medicine and Biology*, vol. 38, pp. 262 –275, 2012.

[17] Y. Huang and D. Chen, “Watershed segmentation for breast tumor in 2-D sonography,” *Ultrasound in Medicine and Biology*, vol. 30, pp. 625 –623, 2004.

[18] D. Boukerroui, A. Baskurt, J. A. Noble, and O. Basset, “Segmentation of ultrasound images - multiresolution 2D and 3D algorithm based on global and local statistics,” *Pattern Recognition Letters*, vol. 24, pp. 779 –790, 2003.

[19] B. Liu, H. Cheng, J. Huang, J. Tian, J. Liu, and J. Tang, “Automated segmentation of ultrasonic breast lesions using statistical texture classification and active contour based on probability distance,” *Ultrasound in Medicine and Biology*, vol. 35, pp. 1309 –1324, 2008.

[20] L. He, Z. Peng, B. Everding, X. Wang, C. Han, K. Weiss, and W. Wee, “A comparative study of deformable contour methods on medical image segmentation,” *Image and Vision Computing*, vol. 26, pp. 141 –163, 2008.

[21] H. D. Cheng, J. Shan, W. Ju, Y. Guo, and L. Zhang, "Automated breast cancer detection and classification using ultrasound images: A survey," *Pattern Recognition*, vol. 43, pp. 299 –317, 2010.

[22] A. Rodtook and S. Makhanov, "Multi-feature gradient vector flow snakes for adaptive segmentation of the ultrasound images of breast cancer," *Journal of Visual Communication and Image Representation*, vol. 24, pp. 1414 –1430, 2013.

[23] Y. Guo, A. ngr, and J.-W. Tian, "A novel breast ultrasound image segmentation algorithm based on neutrosophic similarity score and level set," *Computer Methods and Programs in Biomedicine*, vol. 123, pp. 43 –53, 2016.

[24] D. Gupta and R. Anand, "A hybrid edge-based segmentation approach for ultrasound medical images," *Biomedical Signal Processing and Control*, vol. 123, pp. 43 –53, 2016.

[25] Q.-H. Huang, S.-Y. Lee, L.-Z.Liu, M.-H. Lu, L.-W. Jin, and A.-H. Li, "A robust graph-based segmentation method for breast tumors in ultrasound images.," *Ultrasonics*, vol. 52, pp. 266 –275, 2012.

[26] P. Gu, W.-M. Lee, M. Roubidoux, J.Yuan, X.Wang, and P. L. Carson, "Automated 3D ultrasound image segmentation to aid breast cancer image interpretation," *Ultrasonics*, vol. 65, pp. 51 –58, 2016.

[27] Y. Feng, F. Dong, X. Xia, C. H. Hu, Q. Fan, Y. Hu, M. Gao, and S. Mutic, "An adaptive fuzzy c-means method utilizing neighboring information for breast tumor segmentation in ultrasound images," *Medical Physics*, vol. 44, pp. 3752 –3760, 2017.

[28] Y. Wang, J. Liang, and Y. Jia, "On the critical point of gradient vector flow snake," in *Computer Vision – ACCV 2007: 8th Asian Conference on Computer Vision, Tokyo, Japan, November 18-22, 2007, Proceedings, Part II*. Springer Berlin Heidelberg, 2007, pp. 754–763.

[29] H. Yuan, L. Yupin, and H. Dongcheng, "Semi-automatic initialization of gradient vector flow snakes," *Journal of Electronic Imaging*, vol. 15, no. 4, pp. 043 006–8, 2006.

[30] C.-F. Shu and R. C. Jain, "Vector field analysis for oriented patterns," *IEEE Transactions on Pattern Analysis and Machine Intelligence*, vol. 16, no. 9, pp. 946–950, 1994.

[31] I. Cohen and I. Herlin, “A motion computation and interpretation framework for oceanographic satellite images,” in *Proceedings of International Symposium on Computer Vision - ISCV*, 1995, pp. 13–18.

[32] J. Li, W.-Y. Yau, and H. Wang, “Combining singular points and orientation image information for fingerprint classification,” *Pattern Recognition*, vol. 41, no. 1, pp. 353 –366, 2008.

[33] ——, “Constrained nonlinear models of fingerprint orientations with prediction,” *Pattern Recognition*, vol. 39, no. 1, pp. 102 –114, 2006.

[34] X. Tian, S. Sammaraighe, and G. Murphy, “An integrated algorithm for detecting position and size of knots on logs using texture analysis,” in *Image and Visions Computing*, 1999, pp. 121–132.

[35] W.-Y. Yau, J. Li, and H. Wang, “Nonlinear phase portrait modeling of fingerprint orientation,” in *ICARCV 2004 8th Control, Automation, Robotics and Vision Conference, 2004.*, vol. 2, 2004, 1262–1267 Vol. 2.

[36] N. Ray, S. T. Acton, T. Altes, E. E. de Lange, and J. R. Brookeman, “Merging parametric active contours within homogeneous image regions for mri-based lung segmentation,” *IEEE Transactions on Medical Imaging*, vol. 22, no. 2, pp. 189–199, 2003.

[37] B. N. Saha, N. Ray, and H. Zhang, “Snake validation: A pca-based outlier detection method,” *IEEE Signal Processing Letters*, vol. 16, no. 6, pp. 549–552, 2009.

[38] C.-Y. Hsu, C.-Y. Liu, and C.-M. Chen, “Automatic segmentation of liver {pet} images,” *Computerized Medical Imaging and Graphics*, vol. 32, no. 7, pp. 601 –610, 2008.

[39] C.-Y. Hsu, H.-F. Wang, H.-C. Wang, and K.-K. Tseng, “Automatic extraction of face contours in images and videos,” *Future Generation Computer Systems*, vol. 28, no. 1, pp. 322 –335, 2012.

[40] E. Veronese, R. Stramare, A. Campion, B. Raffeiner, V. Beltrame, E. Scagliori, A. Coran, L. Ciprian, U. Fiocco, and E. Grisan, “Improved detection of synovial boundaries in ultrasound examination by using a cascade of active-contours,” *Medical Engineering & Physics*, vol. 35, no. 2, pp. 188 –194, 2013.

[41] K. Kirimasthong, A. Rodtook, U. Chaumrattanakul, and S. S. Makhanov, “Phase portrait analysis for automatic initialization of multiple snakes for segmentation of the ultrasound images of breast cancer,” *Pattern Analysis and Applications*, vol. 20, no. 1, pp. 239–251, 2017.

[42] D. J. Doshi, D. E. March, G. M. Crisi, and B. F. Coughlin, “Complex cystic breast masses: Diagnostic approach and imaging-pathologic correlation,” *RadioGraphics*, vol. 27, no. suppl_1, S53–S64, 2007.

[43] I.-S. Jung, D. Thapa, and G.-N. Wang, “Automatic segmentation and diagnosis of breast lesions using morphology method based on ultrasound,” in *Fuzzy Systems and Knowledge Discovery: Second International Conference, FSKD 2005, Changsha, China, August 27-29, 2005, Proceedings, Part II*. Springer Berlin Heidelberg, 2005, pp. 1079–1088.

[44] A. Madabhushi and D. N. Metaxas, “Combining low-, high-level and empirical domain knowledge for automated segmentation of ultrasonic breast lesions,” *IEEE Transactions on Medical Imaging*, vol. 22, no. 2, pp. 155–169, 2003.

[45] S. Selvan and S. S. Devi, “Automatic seed point selection in ultrasound echography images of breast using texture features,” *Biocybernetics and Biomedical Engineering*, vol. 35, no. 3, pp. 157 –168, 2015.

[46] K. Fergani, D. Lui, C. Scharfenberger, A. Wong, and D. Clausi, “Hybrid structural and texture distinctiveness vector field convolution for region segmentation,” *Computer Vision and Image Understanding*, vol. 125, pp. 85 –96, 2014.

[47] S. Liu and Y. Peng, “A local region-based chan-vese model for image segmentation,” *Pattern Recognition*, vol. 45, no. 7, pp. 2769 –2779, 2012.

[48] Y. S. Akgul, C. Kambhamettu, and M. Stone, “Extraction and tracking of the tongue surface from ultrasound image sequences,” in *Proceedings. 1998 IEEE Computer Society Conference on Computer Vision and Pattern Recognition (Cat. No.98CB36231)*, 1998, pp. 298–303.

[49] V. Corsetti, N. Houssami, M. Ghirardi, A. Ferrari, M. Speziani, S. Bellarosa, G. Remida, C. Gasparotti, E. Galligioni, and S. Ciatto, “Evidence of the effect of adjunct ultrasound

screening in women with mammography-negative dense breasts: Interval breast cancers at 1 year follow-up," *European Journal of Cancer*, vol. 47, no. 7, pp. 1021 –1026, 2011.

[50] V. Corsetti, N. Houssami, A. Ferrari, M. Ghirardi, S. Bellarosa, O. Angelini, C. Bani, P. Sardo, G. Remida, E. Galligioni, and S. Ciatto, "Breast screening with ultrasound in women with mammography-negative dense breasts: Evidence on incremental cancer detection and false positives, and associated cost," *European Journal of Cancer*, vol. 44, no. 4, pp. 539 –544, 2008.

[51] Y. Wu, Y. Wang, and Y. Jia, "Adaptive diffusion flow active contours for image segmentation," *Computer Vision and Image Understanding*, vol. 117, no. 10, pp. 1421–1435, 2013.

[52] W. Liu, J. A. Zagzebski, T. Varghese, C. R. Dyer, U. Techavipoo, and T. J. Hall, "Segmentation of elastographic images using a coarse-to-fine active contour model," *Ultrasound in Medicine & Biology*, vol. 32, no. 3, pp. 397 –408, 2006.

[53] WHO, *Breast cancer: Prevention and control*, `http://www.who.int/cancer/detection/breastcancer/en/`, Dec. 2016.

[54] M. K. Shetty, "Screening and diagnosis of breast cancer in low-resource countries: What is state of the art?" *Seminars in Ultrasound, {CT} and {MRI}*, vol. 32, no. 4, pp. 300 –305, 2011, Breast Cancer Screening and Diagnosis: State of the Art.

[55] N. S. E. Saghir, C. A. Adebamowo, B. O. Anderson, R. W. Carlson, P. A. Bird, M. Corbex, R. A. Badwe, M. A. Bushnaq, A. Eniu, J. R. Gralow, J. K. Harness, R. Masetti, F. Perry, M. Samiei, D. B. Thomas, B. Wiafe-Addai, and E. Cazap, "Breast cancer management in low resource countries (lrcs): Consensus statement from the breast health global initiative," *The Breast*, vol. 20, Supplement 2, S3 –S11, 2011.

[56] I. Mittra, "Breast cancer screening in developing countries," *Preventive Medicine*, vol. 53, no. 3, pp. 121 –122, 2011, Special Section: Breast Cancer Screening.

[57] L. Foxcroft, E. Evans, and A. Porter, "The diagnosis of breast cancer in women younger than 40," *The Breast*, vol. 13, no. 4, pp. 297 –306, 2004.

[58] M. Yagtu, E. Turan, and C. O. Turan, "The role of ultrasonographic elastography in the differential diagnosis of breast masses and its contribution to classical ultasonographic evaluation," *J Breast Health*, vol. 10, pp. 141 –146, 2014.

[59] A. Itoh, E. Ueno, E. Tohno, H. Kamma, H. Takahashi, T. Shiina, M. Yamakawa, and T. Matsumura, “Breast disease: Clinical application of us elastography for diagnosis,” *Radiology*, vol. 239, pp. 341 –350, 2006.

[60] A. Athanasiou, A. Tardivon, M. Tanter, B. Sigal-Zafrani, J. Bercoff, T. Deffieux, J.-L. Gennisson, M. Fink, and S. Neuenschwander, “Breast lesions: Quantitative elastography with supersonic shear imagingłreliminary results,” *Radiology*, vol. 256, pp. 297 – 303, 2010.

[61] W. A. Berg, D. O. Cosgrove, C. J. Dor, F. K. W. Schfer, W. E. Svensson, R. J. Hooley, R. Ohlinger, E. B. Mendelson, C. Balu-Maestro, M. Locatelli, C. Tourasse, B. C. Cavanaugh, V. Juhan, A. T. Stavros, A. Tardivon, J. Gay, J.-P. Henry, and C. Cohen-Bacrie, “Shear-wave elastography improves the specificity of breast us: The be1 multinational study of 939 masses,” *Radiology*, vol. 262, pp. 435 –449, 2012.

[62] W. K. Moon, J.-G. Im, D.-Y. Noh, and M. C. Han, “Nonpalpable breast lesions: Evaluation with power doppler us and a microbubble contrast agentłnitial experience,” *Radiology*, vol. 217, no. 1, pp. 240–246, 2000.

[63] Y. Yamakoshi, T. Nakajima, T. Kasahara, M. Yamazaki, R. Koda, and N. Sunaguchi, “Shear wave imaging of in vivo breast tissue by color doppler shear wave elastography,” *IEEE Transactions on Ultrasonics, Ferroelectrics, and Frequency Control*, vol. PP, no. 99, pp. 1–1, 2016.

[64] R. Ibrahim, K. Rahmat, F. Fadzli, F. I. Rozalli, C. J. Westerhout, K. Alli, A. Vijayananthan, and F. Moosa, “Evaluation of solid breast lesions with power doppler: Value of penetrating vessels as a predictor of malignancy,” *Singapore Med J*, vol. 57, no. 11, pp. 634–640, 2016.

[65] Y. Davoudi, B. Borhani, M. P. Rad, and N. Matin, “The role of Doppler sonography in distinguishing malignant from benign breast lesions,” *Journal of Medical Ultrasound*, vol. 22, no. 2, pp. 92 –95, 2014.

[66] G. Gokalp, U. Topal, and E. Kizilkaya, “Power Doppler sonography: Anything to add to BI-RADS US in solid breast masses?” *European Journal of Radiology*, vol. 70, no. 1, pp. 77 –85, 2009.

[67] A. Thomas, M. Warm, M. Hoopmann, F. Diekmann, and T. Fischer, “Tissue Doppler and strain imaging for evaluating tissue elasticity of breast lesions,” *Academic Radiology*, vol. 14, no. 5, pp. 522–529, 2007.

[68] L. Li, X. Zhou, X. Zhao, S. Hao, J. Yao, W. Zhong, and H. Zhi, “B-mode ultrasound combined with color Doppler and strain elastography in the diagnosis of non-mass breast lesions: A prospective study,” *Ultrasound in Medicine and Biology*, vol. 43, no. 11, pp. 2582–2590, 2017.

[69] A. Elkharbotly and H. M. Farouk, “Ultrasound elastography improves differentiation between benign and malignant breast lumps using b-mode ultrasound and color Doppler,” *The Egyptian Journal of Radiology and Nuclear Medicine*, vol. 46, no. 4, pp. 1231 – 1239, 2015.

[70] D. Geoff, *Biomedical image processing: Technuques and applications.* Tennessee: Spinger Science & Business media, 2011.

[71] K. S. S. Bhatia, A. C. L. Lam, S. W. A. Pang, D. Wang, and A. T. Ahuja, “Feasibility study of texture analysis using ultrasound shear wave elastography to predict malignancy in thyroid nodules,” *Ultrasound in Medicine & Biology*, vol. 42, no. 7, pp. 1671 –1680, 2016.

[72] Q. Zhang, Y. Xiao, W. Dai, J. Suo, C. Wang, J. Shi, and H. Zheng, “Deep learning based classification of breast tumors with shear-wave elastography,” *Ultrasonics*, vol. 72, pp. 150 –157, 2016.

[73] Y.-L. Huang, S.-J. Kuo, C.-C. Hsu, H.-S. Tseng, Y.-H. Hsiao, and D.-R. Chen, “Computer-aided diagnosis for breast tumors by using vascularization of 3-d power doppler ultrasound,” *Ultrasound in Medicine & Biology*, vol. 35, no. 10, pp. 1607 –1614, 2009.

[74] Y.-H. Hsiao, Y.-L. Huang, S.-J. Kuo, W.-M. Liang, S.-T. Chen, and D.-R. Chen, “Characterization of benign and malignant solid breast masses in harmonic 3d power doppler imaging,” *European Journal of Radiology*, vol. 71, no. 1, pp. 89 –95, 2009.

[75] Y.-C. Chang, Y.-H. Huang, C.-S. Huang, and R.-F. Chang, “Vascular morphology and tortuosity analysis of breast tumor inside and outside contour by 3-d power doppler ultrasound,” *Ultrasound in Medicine & Biology*, vol. 38, no. 11, pp. 1859 –1869, 2012.

[76] Y.-C. Lai, Y.-S. Huang, D.-W. Wang, C.-M. Tiu, Y.-H. Chou, and R.-F. Chang, "Computer-aided diagnosis for 3-d power doppler breast ultrasound," *Ultrasound in Medicine & Biology*, vol. 39, no. 4, pp. 555 –567, 2013.

[77] L. D. Cohen, "On active contour models and balloons," *CVGIP: Image Underst.*, vol. 53, no. 2, pp. 211–218, Mar. 1991.

[78] N. Ray and S. T. Acton, "Motion gradient vector flow: An external force for tracking rolling leukocytes with shape and size constrained active contours," *IEEE Transactions on Medical Imaging*, vol. 23, no. 12, pp. 1466–1478, 2004.

[79] B. Li and S. T. Acton, "Active contour external force using vector field convolution for image segmentation," *IEEE Transactions on Image Processing*, vol. 16, no. 8, pp. 2096–2106, 2007.

[80] V. Caselles, R. Kimmel, and G. Sapiro, "Geodesic active contours," *International Journal of Computer Vision*, vol. 22, no. 1, pp. 61–79, 1997.

[81] T. F. Chan and L. A. Vese, "Active contours without edges," *IEEE Transactions on Image Processing*, vol. 10, no. 2, pp. 266–277, 2001.

[82] C. Li, C. Y. Kao, J. C. Gore, and Z. Ding, "Minimization of region-scalable fitting energy for image segmentation," *IEEE Transactions on Image Processing*, vol. 17, no. 10, pp. 1940–1949, 2008.

[83] X. Xie and M. Mirmehdi, "Mac: Magnetostatic active contour model," *IEEE Transactions on Pattern Analysis and Machine Intelligence*, vol. 30, no. 4, pp. 632–646, 2008.

[84] M. Kass, A. Witkin, and D. Terzopoulos, "Snakes: Active contour models," *INTERNATIONAL JOURNAL OF COMPUTER VISION*, vol. 1, no. 4, pp. 321–331, 1988.

[85] W. Neuenschwander, P. Fua, G. Szekely, and O. Kubler, *Initializing snakes [object delineation]*, 1994.

[86] T. McInerney and D. Terzopoulos, "A dynamic finite element surface model for segmentation and tracking in multidimensional medical images with application to cardiac 4d image analysis," *Computerized Medical Imaging and Graphics*, vol. 19, no. 1, pp. 69 –83, 1995.

[87] L. D. Cohen and I. Cohen, “Finite-element methods for active contour models and balloons for 2-d and 3-d images,” *IEEE Transactions on Pattern Analysis and Machine Intelligence*, vol. 15, no. 11, pp. 1131–1147, 1993.

[88] A. Benson and D. J. Evans, “Algorithm 512: A normalized algorithm for solution of positive definite symmetric quindiagonal systems of linear equations [f4],” *ACM Trans. Math. Softw.*, vol. 3, no. 1, pp. 96–103, Mar. 1977.

[89] A. Chakraborty, L. H. Staib, and J. S. Duncan, “Deformable boundary finding in medical images by integrating gradient and region information,” *IEEE Transactions on Medical Imaging*, vol. 15, no. 6, pp. 859–870, 1996.

[90] J.-Y. Park, T. McInerney, D. Terzopoulos, and M.-H. Kim, “A non-self-intersecting adaptive deformable surface for complex boundary extraction from volumetric images,” *Computers & Graphics*, vol. 25, no. 3, pp. 421 –440, 2001.

[91] T. McInemey and D. Terzopoulos, “Topology adaptive deformable surfaces for medical image volume segmentation,” *IEEE Transactions on Medical Imaging*, vol. 18, no. 10, pp. 840–850, 1999.

[92] J. Cheng and S. W. Foo, “Dynamic directional gradient vector flow for snakes,” *IEEE Transactions on Image Processing*, vol. 15, no. 6, pp. 1563–1571, 2006.

[93] M. Wei, Y. Zhou, and M. Wan, “A fast snake model based on non-linear diffusion for medical image segmentation,” *Computerized Medical Imaging and Graphics*, vol. 28, no. 3, pp. 109 –117, 2004.

[94] N. Jifeng, W. Chengke, L. Shigang, and Y. Shuqin, “Ngvf: An improved external force field for active contour model,” *Pattern Recognition Letters*, vol. 28, no. 1, pp. 58 –63, 2007.

[95] L. Guillot and C. Le Guyader, “Extrapolation of vector fields using the infinity laplacian and with applications to image segmentation,” in *Scale Space and Variational Methods in Computer Vision: Second International Conference, SSVM 2009, Voss, Norway, June 1-5, 2009. Proceedings*. Springer Berlin Heidelberg, 2009, pp. 87–99.

[96] Y. Wang, Y. Jia, and L. Liu, “Harmonic gradient vector flow external force for snake model,” *Electronics Letters*, vol. 44, no. 2, pp. 105–106, 2008.

[97] J. Cheng and S. W. Foo, “Dynamic directional gradient vector flow for snakes,” *IEEE Transactions on Image Processing*, vol. 15, no. 6, pp. 1563–1571, 2006.

[98] A. Rodtook and S. S. Makhanov, “Multi-feature gradient vector flow snakes for adaptive segmentation of the ultrasound images of breast cancer,” *Journal of Visual Communication and Image Representation*, vol. 24, no. 8, pp. 1414 –1430, 2013.

[99] G. Zhu, S. Zhang, Q. Zeng, and C. Wang, “Gradient vector flow active contours with prior directional information,” *Pattern Recognition Letters*, vol. 31, no. 9, pp. 845 –856, 2010.

[100] M. N. Shirazi and Y. Kamakura, *Restructuring centipedes and their applications to fast extraction of structures in electron microscope tomography images*, 2010.

[101] C. Revol and M. Jourlin, “A new minimum variance region growing algorithm for image segmentation,” *Pattern Recognition Letters*, vol. 18, no. 3, pp. 249 –258, 1997.

[102] K. Jensen and D. Anastassiou, “Subpixel edge localization and the interpolation of still images,” *IEEE Transactions on Image Processing*, vol. 4, no. 3, pp. 285–295, 1995.

[103] W. Dong, N. Zhou, J.-C. Paul, and X. Zhang, “Optimized image resizing using seam carving and scaling,” *ACM Trans. Graph.*, vol. 28, no. 5, 125:1–125:10, Dec. 2009.

[104] F. L. Bookstein, “Principal warps: Thin-plate splines and the decomposition of deformations,” *IEEE Transactions on Pattern Analysis and Machine Intelligence*, vol. 11, no. 6, pp. 567–585, 1989.

[105] C. Keatmanee, S. S. Makhanov, K. Kotani, W. Lohitvisate, and S. S. Thongvigitmanee, “Automatic initialization for active contour model in breast cancer detection utilizing conventional ultrasound and color doppler,” in *2017 39th Annual International Conference of the IEEE Engineering in Medicine and Biology Society (EMBC)*, 2017, pp. 3248–3251.

[106] J. C. Bezdek, *Pattern recognition with fuzzy objective function algorithms*. Norwell, MA, USA: Kluwer Academic Publishers, 1981.

[107] P. C. Mahalanobis, “On the generalized distance in statistics,” *Proceedings of the National Institute of Sciences (Calcutta)*, vol. 2, pp. 49–55, 1936.

[108] C. R. Maurer, R. Qi, V. Raghavan, and S. Member, “A linear time algorithm for computing exact euclidean distance transforms of binary images in arbitrary dimensions,” *IEEE Transactions on Pattern Analysis and Machine Intelligence*, pp. 265–270, 2003.

[109] D. P. Huttenlocher, W. J. Rucklidge, and G. A. Klanderman, “Comparing images using the hausdorff distance under translation,” in *Proceedings 1992 IEEE Computer Society Conference on Computer Vision and Pattern Recognition*, 1992, pp. 654–656.

[110] M. P. Dubuisson and A. K. Jain, “A modified hausdorff distance for object matching,” in *Proceedings of 12th International Conference on Pattern Recognition*, vol. 1, 1994, 566–568 vol.1.

[111] D. P. Huttenlocher, G. A. Klanderman, and W. J. Rucklidge, “Comparing images using the hausdorff distance,” *IEEE Transactions on Pattern Analysis and Machine Intelligence*, vol. 15, no. 9, pp. 850–863, 1993.

[112] Matlab, *Fitctree function, the fit binary classification decision tree for multiclass classification*, `https://ch.mathworks.com/help/stats/fitctree.html`, Oct. 2017.

[113] L. Breiman, J. Friedman, R. Olshen, and C. Stone, *Classification and Regression Trees*. Monterey, CA: Wadsworth and Brooks, 1984.

[114] D. Coppersmith, S. Hong, and J. R.M. Hosking, “Partitioning nominal attributes in decision trees,” vol. 3, pp. 197–217, Jan. 1999.

[115] W.-Y. Loh, “Regression trees with unbiased variable selection and interaction detection,” vol. 12, pp. 361–386, Apr. 2002.

[116] W.-Y. Loh and Y.-S Shin, “Split selection methods for classification trees,” vol. 7, pp. 815–840, Oct. 1997.

[117] M. P. Dubuisson and A. K. Jain, “A modified hausdorff distance for object matching,” in *Proceedings of 12th International Conference on Pattern Recognition*, vol. 1, 1994, 566–568 vol.1.

[118] A. Taha and A. Hanbury, “Metrics for evaluating 3D medical image segmentation: Analysis, selection, and tool,” *BMC Medical Imaging*, pp. 15 –29, 2015.

[119] D. Adler, P. Carson, J. Rubin, D Quinn-Reid, C. Kanan, and G. Cottrell, "Doppler ultrasound color flow imaging in the study of breast cancer: Preliminary findings," *Ultrasound in Medicine and Biology*, vol. 16, no. 6, pp. 553 –559, 1990.

[120] W. C. Scarfe, A. G. Farman, and P. Sukovic, "Clinical applications of cone-beam computed tomography in dental practice," *J Can Dent Assoc*, vol. 72, no. 1, pp. 75–80, 2006.

[121] W. Jerjes *et al.*, "Risk factors associated with injury to the inferior alveolar and lingual nerves following third molar surgeryłevisited," *Oral Surgery, Oral Medicine, Oral Pathology, Oral Radiology, and Endodontology*, vol. 109, no. 3, pp. 335 –345, 2010.

[122] T. Kondo, S. Ong, and K. W. Foong, "Computer-based extraction of the inferior alveolar nerve canal in 3-d space," *Computer Methods and Programs in Biomedicine*, vol. 76, no. 3, pp. 181 –191, 2004.

[123] S. Saowapak. and N. Walita, "Automatic detection of inferior alveolar nerve canals on ct images," in *Biomedical Circuits and Systems Conference, 2006. BioCAS 2006. IEEE*, 2006, pp. 142–145.

[124] N. Hanssen *et al.*, "Nerves - level sets for interactive 3d segmentation of nerve channels," in *Biomedical Imaging: Nano to Macro, 2004. IEEE International Symposium on*, 2004, 201–204 Vol. 1.

[125] G. Tognola *et al.*, "Gradient-vector-flow snake method for quantitative image reconstruction applied to mandibular distraction surgery," *Instrumentation and Measurement, IEEE Transactions on*, vol. 58, no. 7, pp. 2087–2093, 2009.

[126] N. L. Gerlach *et al.*, "Evaluation of the potential of automatic segmentation of the mandibular canal using cone-beam computed tomography," *British Journal of Oral and Maxillofacial Surgery*, vol. 52, no. 9, pp. 838 –844, 2014.

[127] G. Kim *et al.*, "Automatic extraction of inferior alveolar nerve canal using feature-enhancing panoramic volume rendering," *Biomedical Engineering, IEEE Transactions on*, vol. 58, no. 2, pp. 253–264, 2011.

[128] R. Llorns, V. Naranjo, F. Lpez, and M. Alcaiz, "Jaw tissues segmentation in dental 3d {ct} images using fuzzy-connectedness and morphological processing," *Computer Methods and Programs in Biomedicine*, vol. 108, no. 2, pp. 832 –843, 2012.

[129] M. Kass, A. Witkin, and D. Terzopoulos, “Snakes: Active contour models,” *International journal of computer vision*, vol. 1, no. 4, pp. 321–331, 1988.

[130] Y. Wu, Y. Wang, and Y. Jia, “Adaptive diffusion flow active contours for image segmentation,” *Computer Vision and Image Understanding*, vol. 117, no. 10, pp. 1421 –1435, 2013.

[131] C. Xu and J. L. Prince, “Snakes, shapes, and gradient vector flow,” *IEEE Transactions on image processing*, vol. 7, no. 3, pp. 359–369, 1998.

[132] ——, “Generalized gradient vector flow external forces for active contours,” *Signal Processing*, vol. 71, no. 2, pp. 131 –139, 1998.

[133] S. Thongvigitmanee *et al.*, “Dentiiscan: The first cone-beam ct scanner for dental and maxillofacial imaging developed in thailand,” in *Nuclear Science Symposium and Medical Imaging Conference (NSS/MIC), 2013 IEEE*, 2013, pp. 1–3.

[134] ——, “Radiation dose and accuracy analysis of newly developed cone-beam ct for dental and maxillofacial imaging,” in *Engineering in Medicine and Biology Society (EMBC), 2013 35th Annual International Conference of the IEEE*, 2013, pp. 2356–2359.

[135] National Electronics and Computer Technology Center: NECTEC, *Dentiview version 3.0*, `http://dentiplan.nectec.or.th/index.php?option=com_content&view=article&id=53&Itemid=61&lang=en`, 2015 (accessed March 12, 2015).

Publications

Journals

[1] Keatmanee, C., Makhanov, S., Kotani, K., Lohitvisate, W., T., Thongvigitmanee, S., Initialization of Active Contours for Segmentation of Breast Cancer via Fusion of Ultrasound, Doppler and Elasticity Images in Ultrasonics.

International Conferences

[2] Keatmanee, C., Makhanov, S., Kotani, K., Kondo, T., Thongvigitmanee, S.,2015. Inferior alveolar canal segmentation in cone beam computed tomography images using an adaptive diffusion flow active contour model, in: the Machine Vision Applications (MVA), 2015 14th IAPR International Confer-ence on, pp. 5760.

[3] Keatmanee, C., Makhanov, S., Kotani, K., Lohitvisate, W., T., Thongvigitmanee, S.,2017. Automatic initialization for active contour model in breast cancer detection utilizing convention ultrasound and Power Doppler, in: the IEEE Engineering in Medicine and Biology Society (EMBC), Seogwipo, 2017, pp. 3248-3251.

[4] Keatmanee, C., Makhanov, S., Kotani, K., Lohitvisate, W., T., Thongvigitmanee, S.,2017. Automatic initialization for active contour model in breast cancer detection utilizing the integration of ultrasonography image modalities, in: SICE annual conference 2017, Kanazawa Japan (September 19-22).

Appendix A

Minor research: Inferior alveolar canal segmentation in cone beam computed tomography images using an adaptive diffusion flow active contour model

The success of dental implant surgery is subject to accurate advanced planning. In order to properly plan for suitable implant placement, it is necessary for accurate segmentation of the inferior alveolar canal. This paper presents a new approach of a semi-automatic method based on a new and effective active contour model viz. an adaptive diffusion flow active contour model. Cone-beam computed tomography (CBCT) images is used as a dataset to extract different views of an inferior alveolar canal. The method has been tested in a ground truth set and evaluated using three similar indicators (the Jaccard index, Dice's coefficient, and Overlap coefficient), achieving promising results in all of them (0.908 ± 0.016, 0.947 ± 0.008, and 0.954 ± 0.008, respectively). Moreover, the presented results show that our method obtains higher accuracy values when compared with GVF snake. The method has proven to be significantly accurate and is possibly integrable in current dental implant surgery planning systems.

A.1 Introduction

A 3-dimensional (3D) dataset acquired from cone-beam computed tomography (CBCT) has become one of the most important dental radiographies for diagnosis of dental and maxillofacial applications [120]. For example, it is applied to dental implant planning: a surgical component which provides an artificial root by means of interfacing with the bone of the jaw (mandible) to support dental prosthesis.

In order to make accurate implant site assessment, the effective visualization system of dental radiography is strongly demanded by dentists. Especially, it could help to reduce the risk of injury to the inferior alveolar nerve (IAN), that affects a sensation system and may cause infection as well as failure to osseointegrate [121]. Due to the position of the IAN traveling within the inferior alveolar canal (IAC) in the mandible, the IAC is more detectable than the IAN itself. Therefore, robust segmentation of the inferior alveolar canal (IAC) is one of the key features to be improved in dental radiography applications.

The aim of this paper is to detect and reconstruct the main feature of IAC using a new and effective active contour model viz. an adaptive diffusion flow active contour model (ADF snake) applied to the CBCT dataset. This paper demonstrates how the algorithm can generate an extremely suitable vector field for a deformable process of the active contour model, to get a well segmented feature of the IAC on each slide of the dataset. Especially, when the IAC passes across the spongious region. Besides segmentation, the ADF snake is applied as a tracking method to get full structure of the IAC in the 3D dataset.

A.2 Related Work and Theoretical Background

Many dental applications have carried out the process of 3D reconstruction from a CT or CBCT dataset by de-emphasizing IAC segmentation as in [122] and [123]; they detected IAC based on panoramic CT images by reforming the stack of original CT images. The segmented results and its visualization of the IAC using the panoramic method may not be very much satisfactory. Another approach [124] presented an IAC based on a geodesic active contour model, the level set method. The main disadvantages of the model is that it has to follow three conditions: the tabular structure consists of only one connected component, not close to other component, and no self-intersections the structure. Beside these conditions, the model may not perform well under the real situation based on the deformable function. A state of the art algorithm, the GVF snake was also implemented in [125] for quantitative image reconstruction applied to mandibular distraction. This paper mostly demonstrated the optimization of the key parameters of the GVF snake as well. Beside the above cited methods, there are various other methods implemented for IAC detection including [126], [127], and [128].

A.3 Theoretical Background

An active contour model [129] has been expansively implemented in image processing and computer vision owing to its proficient performance. Also, there have been many studies that try to overcome its disadvantages including the method applied in this study, a new and effective ADF active contour model (ADF snake). This section aims at simplifying the explanation of an ADF snake as explained below:

An Adaptive Diffusion Active Contour Model

An ADF snake is a new and effective external force [130] developed to solve problems in previous snakes including low capture range, weak edge leaking, as well as deep and narrow concavity regions. This framework is established as an equivalent framework between the GVF snake diffusion process [131] and the image restoration process. The improved features can be described as follows;

For simplicity of theoretical explanation, the GVF energy is rewritten as

$$E(u,v) = \iint \mu \cdot \Phi(|\nabla \vec{v}|) dxdy + \iint |\vec{v} - \nabla f|^2 dxdy. \tag{A-1}$$

1. Weak edge leaking: by considering the GVF snake, in the smoothness energy, the vector field is smoothed in the direction of gradient as same as in the edge direction which is undesired. In order to preserve a weak edge, there should be no diffusion parallel to the gradient. Hence, in ADF *a hypersurface minimal function*: $\Phi(\nabla V) = \sqrt{1 + |\nabla \vec{v}|^2}$ is substituted in the smoothness energy term in the GVF snake. The function is preferable to diffuse along the tangent direction of an edge so that the weak edge is preserved efficiently. When consider $\vec{v}$ as a surface defined on image domain, the corresponding

diffusion term in GVF is given by

$$E(u,v) = \iint \sqrt{1 + |G_\sigma \otimes \nabla \vec{v}|^2} dxdy \tag{A-2}$$

where G_σ is the Gaussian kernel of standard deviation σ which could smooth the vector field, $\nabla \vec{v}$ presents the gradient of $\vec{v}$, and $\otimes$ denotes the convolution operator.

2. Adaptive diffusion force filed: using *harmonic maps*: $p(|\nabla f|) = 1 + 1/(1 + |\nabla G_\sigma \otimes f(x)|)$ which ranges from 1 to 2. Consequently, the diffusion process of the force field can be adjusted adaptively according to image characteristics so it can preserve weak edges and smooth force filed. Thus, the *harmonic hypersurface function* is defined as

$$E(u,v) = \iint \frac{1}{p(|\nabla f|)} (\sqrt{1 + |G_\sigma \otimes \nabla \vec{v}|^2})^{p(|\nabla f|)} d\Omega. \tag{A-3}$$

where Ω is a bounded open subset of $\Re^2$, $\partial\Omega$ denotes its boundary and f presents an edge map.

3. Converge to narrow and deep concavity: developed *Infinity Laplacian function* to encourage the diffusion along the normal direction in the image smoothing region so as to make vectors downward into the boundary concavity instead of converging from two opposite directions. The function is given by

$$E(p \to \infty)(u,v) = \frac{1}{p} \int_\Omega |\nabla \vec{v}|_{L^\infty(\Omega)} d\Omega. \tag{A-4}$$

Finally, a unified diffusion framework, called *adaptive diffusion flow (ADF)* is given by

$$\begin{aligned} E_p(u,v) = & \\ & \iint g \cdot (-m \cdot \Theta_{L^\infty(\Omega)} + (1-m) \cdot \frac{1}{p(|\nabla f|)} \cdot (\sqrt{1+\Omega})^{p(|\nabla f|)}) dxdy \\ & + \iint h \cdot (|\vec{v} - \nabla f|^2) dxdy \end{aligned} \tag{A-5}$$

where $\Theta = |G_\sigma \otimes \nabla \vec{v}|^2$, g and h are weighting functions (same as GGVF [132]); $g(\nabla f) = e^{-(\frac{|\nabla f|}{K})}$ (K is the weighting parameter determining to some extent degree of tradeoff between field smoothness and gradient conformity), $h(|\nabla f|) = 1 - g(|\nabla f|)$, and m is also the weighting function which is given by

$$m = \begin{cases} [1 - f^2/5K^2]^2 & \text{if } f^2/5 \leq K^2 \\ 0 & \text{othervise.} \end{cases}$$

here, $K = 1.4826 \cdot E(||\nabla f| - E(|\nabla f|)|)$ and $E(\cdot)$ presents the mean value.

A.4 Inferior Alveolar Canal Segmentation

Segmentation of an IAC is still challenging due to an imperfect of the dataset (CBCT) including noise, low contrast, and broken boundaries. Especially, when considering all drawbacks of previous methods and the effective performance of the ADF snake as mentioned earlier, the ADF snake stands out to be one of the proficient methods for IAC segmentation.

A.4.1 Materials

The CBCT data were provided by the Dental cone-beam CT Scanner (DentiiScan) [133] and [134]. CBCT volumes are comprised of slices of size 400×400 pixels, with resolutions of $\Delta x = \Delta y = \Delta z = 0.4mm$. The number of slices is 323 in each patient.

A.4.2 Image Enhancement

Based on the imperfect of the dataset, that are noisy, low in contrast, and with broken boundaries, image enhancement is needed before the segmentation process. The morphological operations (top-hat and bottom-hat) were applied to the dataset for edge enhancement and noise suppression as shown in Figure A.1. By leting $f : E \mapsto \Re^2$ be a grayscale image, and $b(x)$ be a grayscale structuring element, the enhanced image is

$$f_{enhance} = f + (f - f \circ b) - (f \bullet b - f).$$

A.4.3 Segmentation and Tracking Process

The significant property of the ADF snake for IAC segmentation is that it can create a suitable vector field for snake deformation based on the image characteristics; for example weak edge, disconnected, and strong adjacent boundaries. The comparison of vector fields and segmented

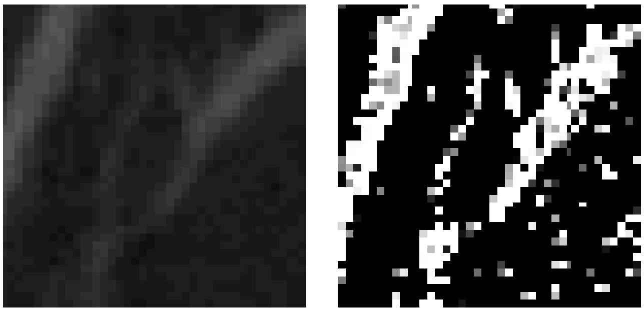

(a) (b)

Figure A.1: An example of IAC enhancement image. (a) Original image.; (b) Enhanced image.

boundaries between well-known algorithms, the GVF snake and the ADF snake are shown in Figure ??. It can be noted the ADF snake performs very much better than the GVF snake. By considering the force field, ADF force field's direction is more parallel to the IAC boundaries than the force field of GVF because the ADF force field is calculated in both normal and tangent directions whereas the GVF force field is computed in only normal direction.

An ADF snake was used for an IAC segmentation, slice by slice, and then reconstruct it for 3D visualization. Besides segmentation, the active contour model has significant performance for object tracking. Therefore, the ADF snake is applied as a tracking method by user intervention in the first and last slices for contour initialization and at the end of tracking process respectively. In between both slices, the ADF snake is applied to the current segmented results to be an initial contour of the next slice. The procedure for the IAC segmentation and tracking is described in the flowchart as shown in Figure A.3.

A.4.4 3D Reconstruction

The segmented CBCT results are visualized in 3D volume rendering by CBCT image viewer: DentiView version 3.0 (NECTEC, Thailand) [135]. An example of 3D reconstruction of a patient's IACs in the right and left sides are shown in Figure A.5.

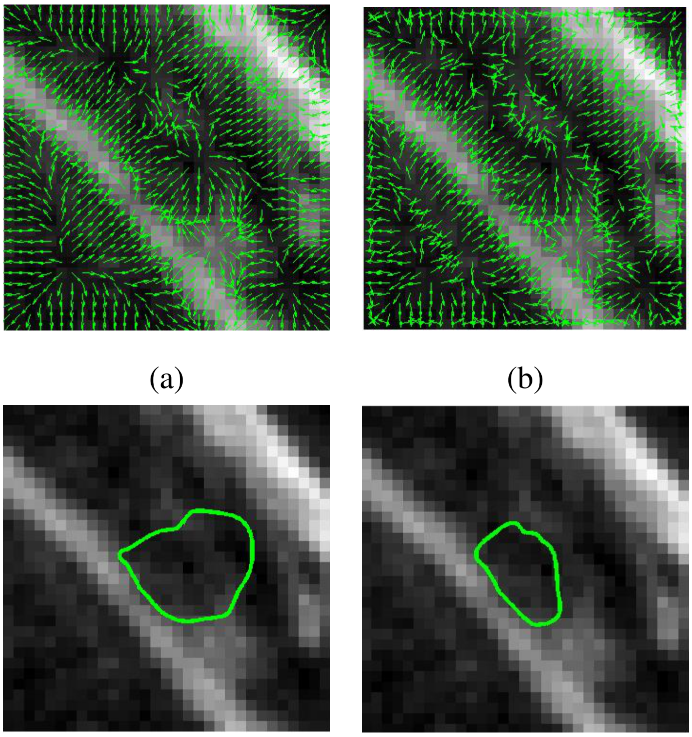

(a) (b)

(c) (d)

Figure A.2: The comparison of IAC segmentation between the GVF snake and the ADF snake focusing on weak edge leaking convergence. (a) GVF force field; (b) ADF force field; (c) GVF snake segmentation result; (d) ADF snake segmentation result; Both models use the same parameters for deformation, $\alpha = 0.1$, $\beta = 1$, $iteration = 60$.

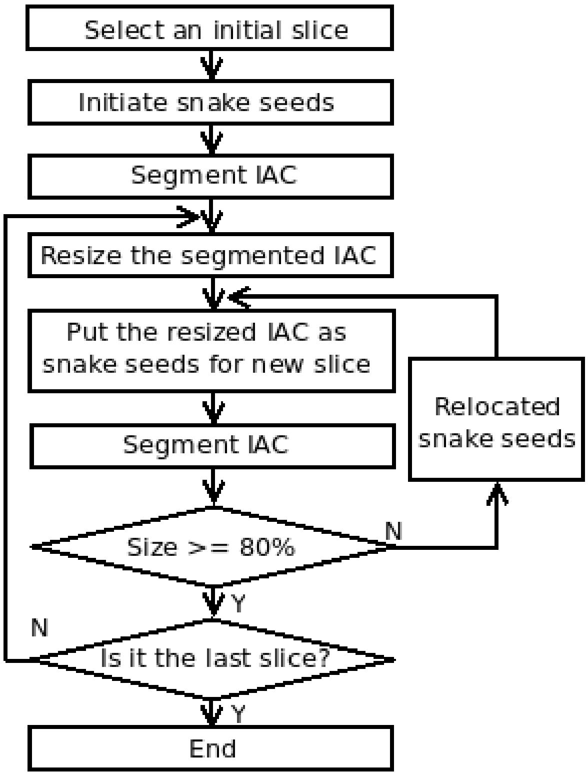

Figure A.3: A flowchart for segmentation and tracking of the ADF snake to find IACs in a 3D dataset.

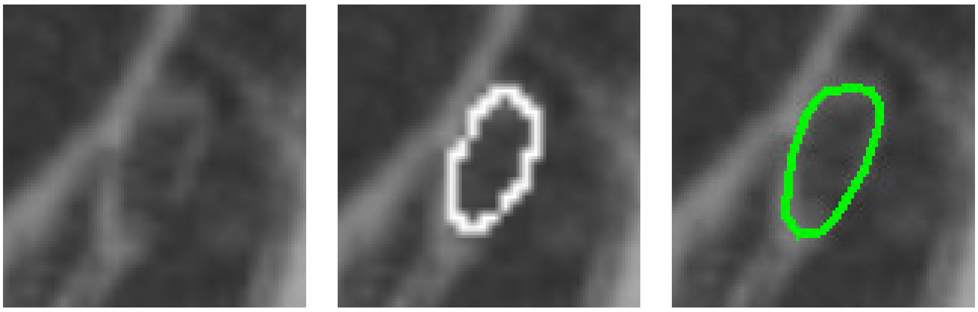
(a) (b) (c)

Figure A.4: An example IAC segmentation by ADF snake and its ground truth. (a) An original IAC image; (b) The bright contour depicts a result of an IAC segmentation by ADF snake ; (c) The apparent contour expresses a ground truth of an IAC.

A.4.5 Data Analysis

In order to evaluate the accuracy of the segmentation process, 6 CBCT data were considered. The ground truth was manually segmented (randomly) in 6 hemimandibles which consisted of 240-303 cross-sections. An example of the segmented result and its ground truth are shown in Figure A.4.

There are 3 different indicators of similarity used for comparing the cross-sections segmented by the proposed method with the ground truth;

- Jaccard index (JI)

$$JI(I_{seg}, I_{gt}) = \frac{|I_{seg} \cap I_{gt}|}{|I_{seg} \cup I_{gt}|}, \text{ where } 0 \leq JI \leq 1$$

- Dice's coefficient (DC)

$$DC(I_{seg}, I_{gt}) = \frac{2|I_{seg} \cap I_{gt}|}{|I_{seg}| + |I_{gt}|}, \text{ where } 0 \leq DC \leq 1$$

- Overlap coefficient (OC)

$$OC(I_{seg}, I_{gt}) = \frac{|I_{seg} \cap I_{gt}|}{min(|I_{seg}|, |I_{gt}|)}, \text{ where } 0 \leq OC \leq 1$$

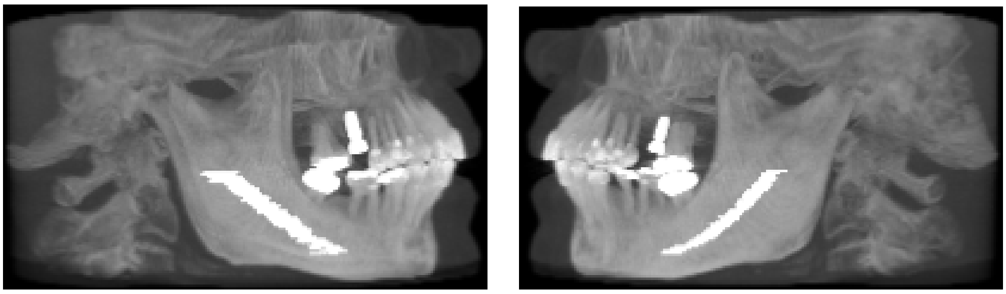

(a) (b)

Figure A.5: 3D reconstruction of IAC from segmented cross-sections. (a) and (b) are the IACs at the right and left sides of the patient.

Table A.1: Mean values for the analyzed indicators.

ADF snake	JI	DC	OC
Mean(μ)	0.9087	0.9472	0.9542
S.D.(σ)	0.0162	0.0087	0.0086
GVF snake			
Mean(μ)	0.7617	0.7998	0.8097
S.D.(σ)	0.0189	0.094	0.0094

A.5 Results and Discussion

The six datasets were measured with 3 similarity indicators as shown in Section A.4.5, and the mean values as well as the standard deviation for all cases are shown in Table A.1.

According to the dataset, the segmentation process is performed in cross-sectional images and the evaluation of the method has focused on studying the 2D segmentation in the cross-sections. Therefore, the evaluation strategy is based on the comparison of processed images with ground truth sets.

The results of the presented method in the described dataset have been promising in all the considered similarity indicators. Considering the overlap indicators, the method has achieved high values in the processed dataset, that is 0.908±0.016, 0.947±0.008, and 0.954±0.008 (in terms of mean value and standard deviation) in the JI, DC, and OC indicators, respectively.

Moreover, the presented results show that our method obtains higher accuracy values when compared with GVF snake.

A.6 Conclusions and Future Work

This paper has proposed a new segmentation approach for CBCT images: The ADF snake for IAC segmentation and reconstruction. The algorithm has been exhaustively measured for three indicators including the Jaccard index, the Dice's coefficient,and the Overlap coefficient. All results indicate achieving of accuracy and thus providing reliable information to computer-aided programs in order to facilitate oral surgery. Future work will focus on full-automatic segmentation with no interfere of end users. Further testing of other segmentation methods is also needed in order to improve accuracy.